Coupled Experimentally-Driven Constraint Functions and Topology Optimization utilized in Design for Additive Manufacturing

by

Ken Mangouh Nsiempba

A thesis
presented to the University of Waterloo
in fulfillment of the
thesis requirement for the degree of
Master of Applied Science
in
Mechanical and Mechatronics Engineering

Waterloo, Ontario, Canada, 2020

Author declaration

I hereby declare that I am the sole author of this thesis. This is a true copy of the thesis, including any required final revisions, as accepted by my examiners.

I understand that my thesis may be made electronically available to the public.

Abstract

Topology optimization (TO) is a structural optimization technique that searches for the proper material distribution inside a design space such that an objective function is maximized/minimized. Rapid prototyping technologies such as additive manufacturing (AM) have allowed results from TO to be manufacturable. However, despite advancements in their ability to manufacture complex geometries, AM technologies still face certain constraints such as printing features at overhangs (unsupported features oriented at a certain angle from the axis normal to the build plate) and small feature sizes, amongst others. In the field of design for additive manufacturing (DfAM), it is common to only restrict one constraint to control the quality of the final parts. However, several studies have found that the final quality of a feature is heavily affected by at least two coupled constraints: the overhanging angle and the feature's thickness. Modifying a structure's layout while restricting only one constraint can uselessly increase the weight of a structure. To tackle this problem, the work done in this thesis considers the interplay between two geometrical constraints. The proposed research reviews some of the essential manufacturing constraints in topology optimization and emphasizes the need for coupling existing constraints. It first develops experiments to obtain a qualitative and a quantitative relationship between the design features' surface qualities, orientation, and thickness. The relation between those parameters is used to update the layout of topologically optimized structures. The layout is changed by obtaining the medial axis of topologically optimized structures and then using implicit functions to conditionally thickening it. Throughout the analysis, it was observed that both the inclination and the thickness affect the surface quality. Furthermore, the effect of the parameters is more pronounced for low thicknesses and higher overhanging angles. The overhanging angle impacts the surface quality more than the thickness, which can be seen through ANOVA.

Acknowledgements

I want to thank all the people who made this achievement possible. I want to start by thanking my parents, who have made their children's blossoming the purpose of their existence. I'd also like to thank my two little sisters for continually pushing me to surpass myself. Then, I'd like to thank my supervisor for providing me with such a fantastic opportunity. Finally, I'd like to thank my colleagues and the MSAM lab staff for their guidance and support.

Dedication

I want to dedicate this work to the family members and the close friends we have recently lost. May their souls rest in peace.

Table of Contents

List of Figures

List of Tables

List of Acronyms

AM	Additive Manufacturing
FE	Finite Elements
FEA	Finite Elements Analysis
FEM	Finite Elements Methods
LSM	Level Set Method
MMA	Method of Moving Asymptotes
MMC	Moving Morphable Components
MMV	Moving Morphable Voids
OA	Overhanging Angle
OC	Optimal Criteria
RAMP	Rational Approximation Material Properties
SIMP	Solid Isotropic Microstructure Penalization
TO	Topology Optimization
TOS	Topologically Optimized Structure
VTM	Virtual Temperature Method

Chapter 1

Introduction

1.1 Additive manufacturing

Additive manufacturing (AM), also referred to as 3D printing, is a manufacturing technique that consists of building parts layer by layer. AM processes have been around since the '80s, but they have had a resurgence in popularity only recently. This resurgence is primarily attributed to the expiration of patents filed in the '80s and has allowed a growing pool of AM users. To print a part, a 3D model is first created, then it is sliced and converted to a G-Code, which is sent to the AM machine. Once the parameters of the machine are configured, the part can be built. It is then removed from the build plate and post-processed.

Its ability to create parts layer by layer has several benefits over traditional manufacturing methods such as casting. First, due to the AM process' nature, the manufacturing cost is associated with the part's volume rather than its complexity. Second, due to the ability to create complex parts, it has allowed "functional design" to flourish. Functional design occurs when the final design of a part reflects its functional requirements rather than its manufacturing limits. Third, because complexity is less of an issue, AM allows more custom parts to be made, which is an attractive feature for domains like medicine. It is also why the advent of AM or 3D printing is often referred to as the "democratization of manufacturing". Despite all of the benefits of technology, there are still some drawbacks. One of the most significant disadvantages is repeatability. Unlike other traditional processes that have been mastered after decades of knowledge and expertise gained, AM is still young, and AM parts quality is usually hard to predict and therefore repeat. In the literature, two avenues are generally discussed to come up with a solution. The first

one is physical modeling; being able to physically model the AM process can be used to predict a part's quality. However, coming up with such a model can sometimes require an understanding of many factors and their mutual interactions. Furthermore, physical modeling and simulation have a high computational cost, which increases as the number of parameters (factors) to evaluate increases. The other solution is statistical modeling. Statistical modeling is helpful when the data is abundant and can help users recognize patterns without understanding the process's physical aspects. Machine learning is one of the statistical modeling tools that becomes a lot handier in cases where there are many parameters to consider. Another problem in 3D printing is that some design features still cannot be manufactured by AM processes. For example, for powder bed fusion processes (which will be discussed more thoroughly in chapter 2), parts cannot have closed holes as that can result in trapped powder particles. The most recurrent design rules are the overhangs and the minimum feature size.

1.2 Topology optimization

Examples of complex parts allowed by 3D printing are found in topology optimization case studies. Topology optimization is a structural optimization method that can be subdivided into two categories, gradient and non-gradient based optimization techniques. This study will focus mostly on gradient-based methods.

Gradient-based methods refer to techniques that rely on minimizing an objective function where the search direction is defined by the derivative of the function at the current point [6]. In the case of the topology optimization method used for this study, the objective function is compliance, which is derived from the strain energy formula. It usually requires several iterations in which design variables are updated until convergence is reached. Initially, finite element analysis (FEA) is carried out on the design space using specific forces and loads. Based on this, a displacement response $\mathbf{U}$ can be obtained for all design variables. The displacement response is used to compute the compliance of each element. The derivative of the compliance and constraint functions is then used to update the elements' densities.

Non-gradient based method are methods which do not require minimizing a function and reaching convergence. Some of the most famous non-gradient based methods are the evolutionary structural optimization (ESO) and the bi-directionality evolutionary structural optimization (BESO).

1.3 Objectives

In recent years, there have been numerous works detailing the integration of manufacturing constraints in the topology optimization procedure; however, those that focused on coupling the constraints[7] have been more scarce. For example, Weiss et al. [8] have described a coupling method that uses experimental data to influence the resulting topologically optimized structures (TOS). To alter the TOS, the design features they chose were parameterized trapezoidal fins. They studied how the minimum allowable fin's thickness varied when changing the fin's length and orientation. This allows more flexibility within the design problem, resulting in more robust design candidates[7]. Despite suggesting using a quantitative approach (dimensional accuracy), the metric they used to describe the printability was qualitative (pass/fail).

The method proposed in this thesis focuses on evaluating how some constraints (design feature's thickness and orientation) are linked through a rigorous set of experiments, which establishes how the constraints can be coupled and used to alter the TOS layout.

In this study, the authors have chosen to use a quantitative metric: the surface roughness of down-facing surfaces, which is related to the features' surface quality. For simplification purposes, less focus has been given to the length of a feature but rather to the thickness and the OA of the feature.

This thesis's statement of objective is the "Development of coupled experimentally-driven constraint functions and Topology optimization for the utilization in design for additive manufacturing".

To this extent, the following objectives are pursued:

- First, the study has to qualify and quantify the impact of the two design parameters on the surface quality of the final manufactured parts.
- Then, the study has to express the surface quality as a function of the two manufacturing constraints.
- The final step is to use that relationship to alter the layout of topologically optimized structures.

1.4 Layout of the thesis

The thesis addresses the issue of part quality in 3D printed parts. To do so, it focuses on specific steps that it aims at achieving simultaneously. The steps of the thesis can be

summarized below:

- Chapter 2 - Literature review:
  The final quality of 3D printed parts has been studied for a long period; hence it is essential to do a global review of the relevant articles from this field. The review will document the attempts that have been made to describe the part qualities by decomposing those parts into design features. Although several studies have designed experiments to understand and quantify the factors that affect 3D printed parts' surface quality, more experiments will still need to be done. The section will also review AM constraints for topology optimization.

- Chapter 3 and 4 - Qualification and quantification of design features' qualities:
  The purpose of this section is to generate more data from which rules can be extracted. To develop a proper experiment, the concept of a design feature will be specified. Several configurations of the design features will be printed and characterized.

- Chapter 5 - Modification of optimized structures layout based on the experimental data:
  The study will then describe how the experimental data can be processed and approximated so that it can be used to modify existing topologically optimized structures.

- Chapter 6 - Conclusions and Future Work:
  Finally, the conclusion will be drawn, and more will be said about future steps.

Chapter 2

Literature review

2.1 Challenges of additive manufacturing

2.1.1 What is additive manufacturing?

AM technologies all have a lot of similarities. First, they all build parts by adding layers on top of each other. They all have an agent that helps shape raw material into viable products. They are all computer-assisted. They differ in the type of materials they can process, the kind of agent (energy source or binding agent) they use, the transformed material's location with respect to the agent, etc... The differences allow users to subdivide them into different categories. In total, seven types have been defined: vat polymerization - which uses photopolymer resin-, material jetting - which creates objects similarly to a two-dimensional inkjet printer-, binder jetting -which uses a binding agent to join layers of powder together-, material extrusion -where the extruder melts the material-, sheet lamination, directed energy deposition and finally powder bed fusion. In this thesis, the latter AM technology has been used. More specifically, laser powder bed fusion (LPBF).

LPBF is a process where a laser is used to melt the 3D model's cross-section onto a powder bed's top powder layer. A re-coating blade is used to add a new layer of powder after each cross-section is done, as shown in figure 2.1.

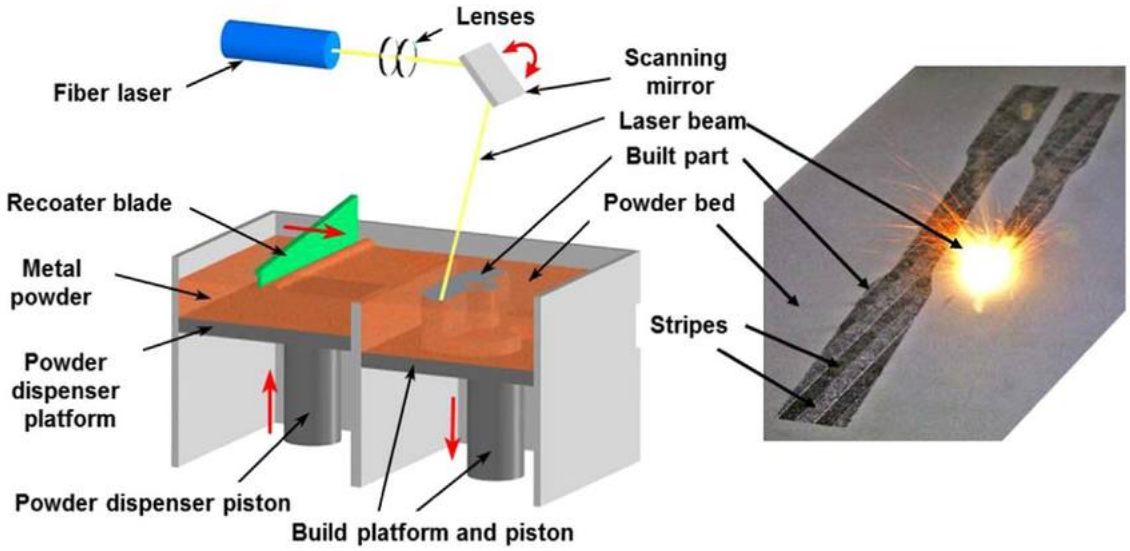

Figure 2.1: Diagram of the laser powder bed fusion process- from EOS-GmbH found in [1]

AM technologies have disrupted the manufacturing industry significantly due to their flexibility and efficiency [9]. The process consists of building a part layer by layer, allowing more complex designs, and saving more materials due to almost zero material waste. Examples of intricate designs include the results of topologically optimized structures. Despite the advancements, AM still has a hard time manufacturing features with large overhanging angles(OAs) (larger than 45°), enclosed voids, and small-sized features, amongst others.

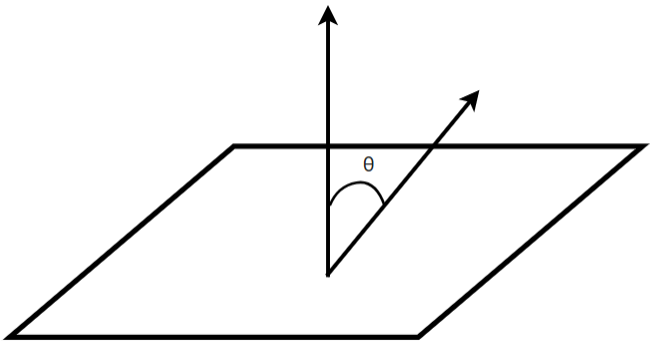

Figure 2.2: Diagram of an overhanging angle θ

2.1.2 Design rules and guidelines for metal additive manufacturing technologies

As discussed by Oropallo and Piegi [10], AM allows the manufacturing of complex geometries; therefore, to explore the full potential of 3D printing, the design process has to be rethought. There are some limits to AM abilities such as the need for post-processing to remove supports, improve surface quality, or finalize certain features. In general, there are multiple approaches to come up with design rules for additive manufacturing. While some are based purely on experimental results [11, 7], some others are based on physical considerations [12, 13].

Experimental approaches

Certain experimental approaches design geometrical features and then print many configurations of them [11, 7]. This method works but is limited since many other parameters (process-wise and material-wise) have to be considered. A few other frameworks have considered process and material parameters. Such studies reveal that the amount of freedom given to geometrical features' configuration depends on the type of process and material parameters. It thus shows how design for additive manufacturing is flexible and highly dependent on non-geometrical parameters. As the number of parameters increases, some have suggested the need for statistical approaches to investigate further the relation between parameters and the end product's manufacturability. It is the case of Wang et al. [14] who have used Bayesian network modeling to infer the impact of design/process/material parameters on the manufacturability of the final product. The limiting factor in AM is the amount of available data on 3D printed parts.

Physics-based approaches

Ideally, physics-based approaches are better predictors, but practically for AM, there are many phenomena to consider. Such phenomena include heat transfer. Some reviews have stressed the importance of understanding how the heat transfer behaves within a part and also how this behavior could influence the part deformation and dimensional accuracy [13]. A few other articles have described how gravity and some process phenomena may affect the dimensional accuracy of specific design features [15].

As physics is often hard to comprehend, design rules are mostly defined by experience. Thus, the industrial sector can contribute a lot more to design since many parts are printed

due to market demand. One of the industrial giants in 3D printing is 3D Hubs, an online platform for 3D printing services. They have come up with common mechanical design features (supported walls, horizontal bridges, etc.) and their minimum allowable dimensions for various AM processes. For example, the minimum hole diameter is 1.5mm. The minimum feature size should be 0.8 mm [16].

The main problem with such rules is that they are dependent on so many other factors. Even when the process parameters are not considered, the size of a feature can be restricted by its overhanging angle and vice versa [7]. Another difficulty is the infinite amount of potential geometrical features candidates. Qualifying them all is an impossible task. Further down, the study will discuss how some of those constraints can be mathematically formulated and integrated into topology optimization programs.

2.1.3 Quantification of design features performance

Quantification of design feature performance has been a recurring problem in manufacturing. Mostly because the problem has two stages; first, the design features have to be defined, and then, they have to be classified. Only then can designers and manufacturers investigate what features are more challenging than others when it comes to manufacturing for a specific process.

Surface roughness

The topic of surface roughness will reoccur many times in this thesis; hence it is crucial to define it first. Surface roughness is a measure of a surface property. It is obtained by measuring all the deviations of a surface from its ideal form. The deviations are in the direction normal to the surface.

However, many parameters can be used to express the surface roughness. One of the most famous is the arithmetical mean deviation of the assessed profile, Ra. To measure Ra, several points are taken on a surface by intervals, and their heights are measured. A mean is computed, and the relative height or depth (distance to the mean surface) at each point i, y_i is obtained [17, 18].

Ra is then defined by the equation below:

$$Ra = \frac{1}{N} \cdot \sum_{i=1}^{N} |y_i| \tag{2.1}$$

where N is the total number of points. The appropriate parameters are shown in figure 2.3.

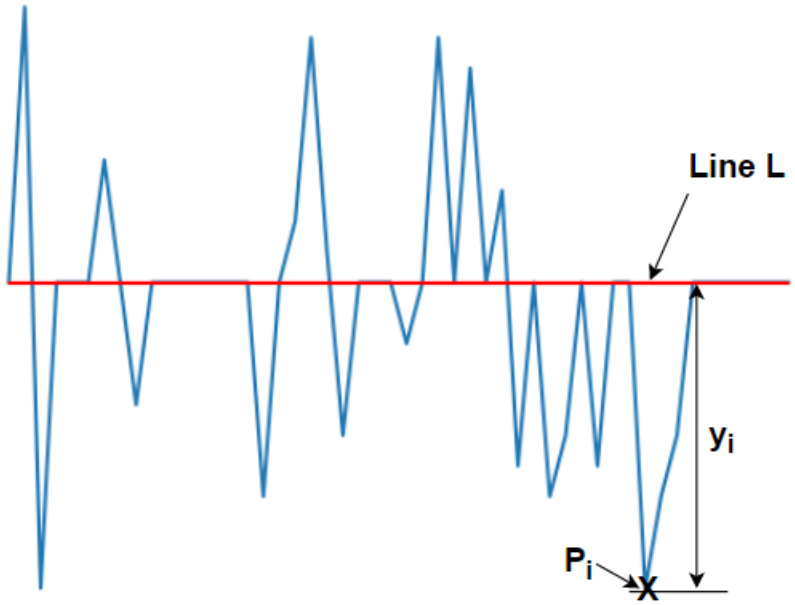

Figure 2.3: Image of a rough surface and a deviation at point i

The surface roughness of parts is important because it often describes the accuracy of a particular manufacturing process. Furthermore, surface roughness can impact additional properties of the parts, such as thermal and mechanical properties. More on it will be discussed later on.

Design features classification approaches

To correctly classify a design feature, one must categorize them twice. The first time, to describe how the shape can be represented, and the second time, to describe how the shape can be recognized. Therefore, a new shape recognition paradigm was generated to decouple shape representation and recognition for this work. Shape representation technics refer to how a shape can be described. For this work, four were identified: volumetric decomposition (decomposition of a shape into subcomponents without any transformation), mathematical representation (representations which have to do with functions or any sort of transforms), graph-based representation (representation of a shape are adjacency graphs, where nodes indicate the sub-shapes and the edges indicate the connection between the sub-shapes) and symbolic representation (methods based on language or syntax).

Then, there are shape recognition methods. Shape recognition can be done mainly analytically, where parts are classified using rules/hints that do not rely on the other parts which ought to be classified, or statistically.

Design features evaluation approaches

Once the shapes are classified, they can then be evaluated. A few examples in literature have done related work, such as the paper from Adam and Zimmer [11]. In the specific paper, Adam and Zimmer came up with several design features, and they proposed several configurations for those design features. Then, using those configurations, they were able to determine their manufacturability through experiments. Other authors have done similar work. The idea is to develop a framework to classify additive manufacturing design features correctly, and then to be able to quantify their performance. In the article by Jee et al. [19], the authors first defined primitives, which are independent parameters. From those primitives (angle of feature, feature size, material type), modules were derived (overhang is a module dependent on feature angle and feature size). Finally, rules were given for the modules based on the primitives' value on which they depend. Mani et al. showed other design guidelines frameworks. In their approach, design rules were derived from design principles, which themselves were derived from design guidelines and design fundamentals [20]. Design rules are restrictions on specific process attributes or feature dimensions. Design principles are basic logical correlations capturing process parameters and control parameters. Finally, design guidelines are qualitative restrictions of design features or process parameters, and design fundamentals refer to groups of parameters(geometry parameters and machine parameters). Also, Wang et al. [14] have advocated for the use of Bayesian networks to understand the effect of design parameters (feature dimensions, feature size), the process parameters (laser power and speed), and the material properties on the resulting properties (surface finish, accuracy) of the part. The recurring issue with most of those articles is the type of features that ought to be analyzed; how does one identify a feature? How is that done for complex, irregular shapes which have been enabled by additive manufacturing?

The results of TOS are often likened to lattice structure. In this study, the expression "design feature" will refer to the trapezoidal shapes that result from the decomposition of the TOS into convex parts (see figure 2.4 and 2.5).

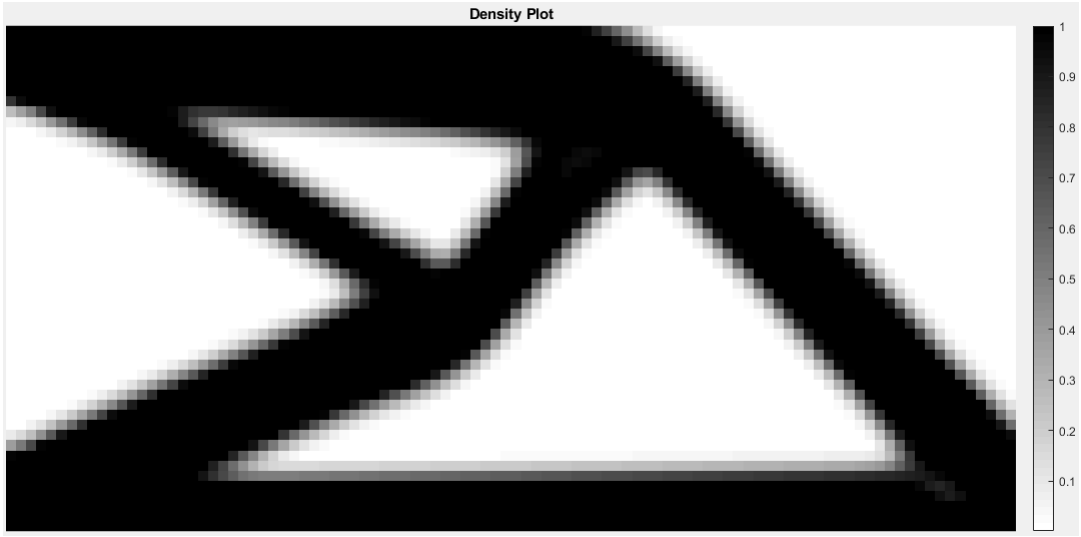

Figure 2.4: Topologically optimized structure. The design space was 50x100 pixels and the force was applied downwards on the right-most bottom-most node

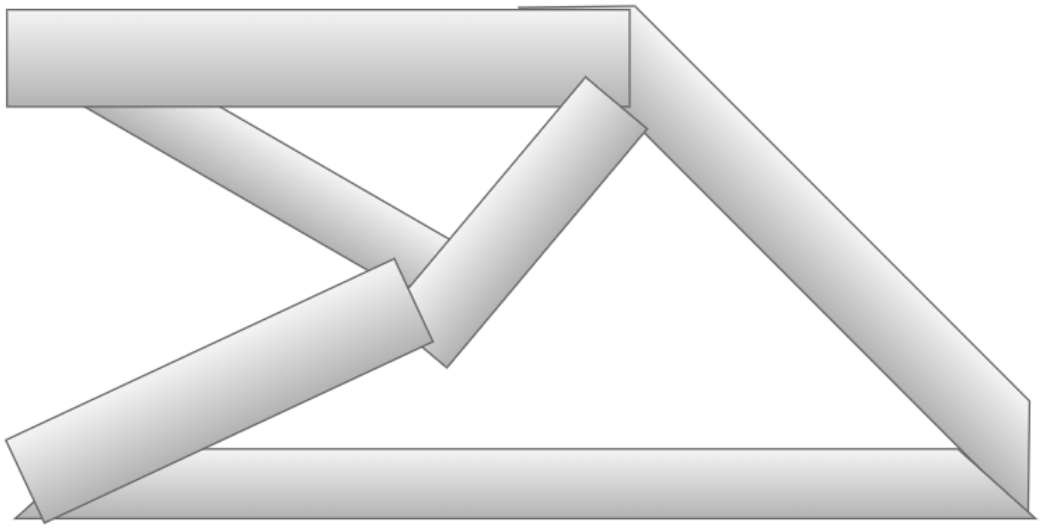
Figure 2.5: Structure of figure 2.4 represented as an assembly trapezoidal shapes

Using that definition of design feature, a lot can be learned in the field of quantification of design features for lattice structures. Hence, the next section will review the efforts that have been put forward to evaluate the printability of lattice structures.

2.1.4 Evaluation lattice structures design features

Lattice structures make an interesting case for design features evaluation because they are made by replicating struts or arrangement of struts and that consequently, for most of the cases, only three design variables can be used to define a strut (diameter, length, and orientation with respect to the XY plane). Therefore, a homogenization process can be used to predict the integrity of the final geometry. Furthermore, there are different possible representations of lattice structures. One could simply be the lattice wireframe, with each line (representing a strut) having as information the radius of the particular strut. This design representation can fall between two different categories amongst the one stated in the previous section. It could be a mathematical one, as it requires a level of abstraction. Still, one could also argue that it would fall in the category of volumetric decomposition as the wireframe can be seen as part of the lattice structure. Furthermore, lattice structures can also be seen as a graph data structure. Graphs are common in the field of computer science. For such a graph-based representation, the struts can be seen as the edges, and the junction of the struts would be seen as the nodes of the graph (see figure 2.8). Each edge could store the length and the radius of the strut as information. The analogy between lattice/truss structures and graphs has been used previously to analyze a lattice structure under loading. The analogy shows that there are many opportunities to represent lattice structures' design features and evaluate them. The next subsection reviews the approaches used to predict lattice structures' properties for specific AM processes.

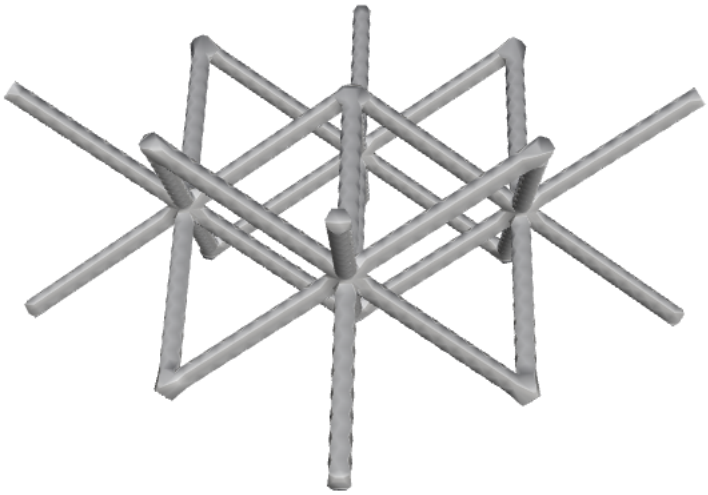

Figure 2.6: Example of a lattice structure

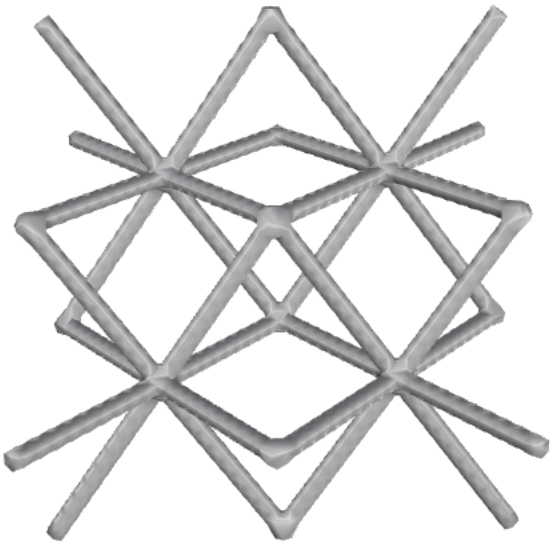

Figure 2.7: Same lattice structure as the one in figure 2.7 under a different angle

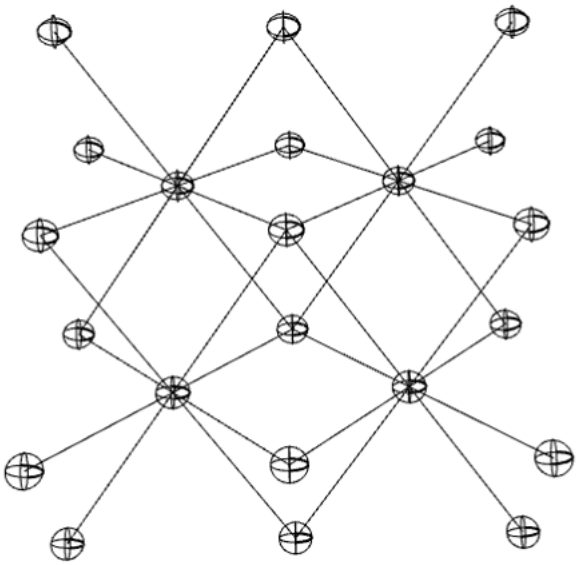

Figure 2.8: Graph based representation of a lattice structure in figures 2.7 and 2.6

Extrusion processes

Park et al. [21] tried to analyze/predict the mechanical properties of cellular materials fabricated by material extrusion. To do this, the authors came up with a method using two transformation stages. The first step consisted of finding the geometrical and material effective properties by estimating an effective strut radius using stochastic methods. The second step was about estimating mechanical properties based on the discretized homogenization method. That method was used for lattice structures. They have found that their method estimated mechanical properties better than other methods.

Two years later, the same authors wrote a paper [2], in which they revealed that lattice structures are much more sensitive to print defects, such as the staircase effect due to the thin struts, as it can be seen in figure 2.9. Their new paper proposed a voxel-based approach to simulate the property degradation. The proposed approach successfully modeled the deposition path and staircase effect. Unfortunately, due to the lack of an interface model, it could not describe tensile strength degradation.

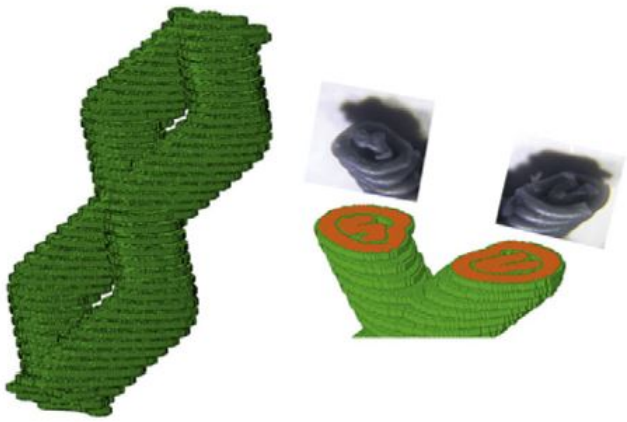

Figure 2.9: Resulting as-fabricated voxel models of printed specimens [2]

Powder bed processes

Suard et al. [3] also suggested using the equivalent diameter to take into account the porosity of the strut. Porous sections do not transmit load as efficiently as solid sections. So therefore, the load supporting area is less than what is printed. Using the equivalent diameter approach, they found FEA simulation results fit well with experimental values

(see figure 2.10). Although many of the works referenced above have addressed the issues, there is still a lot of work.

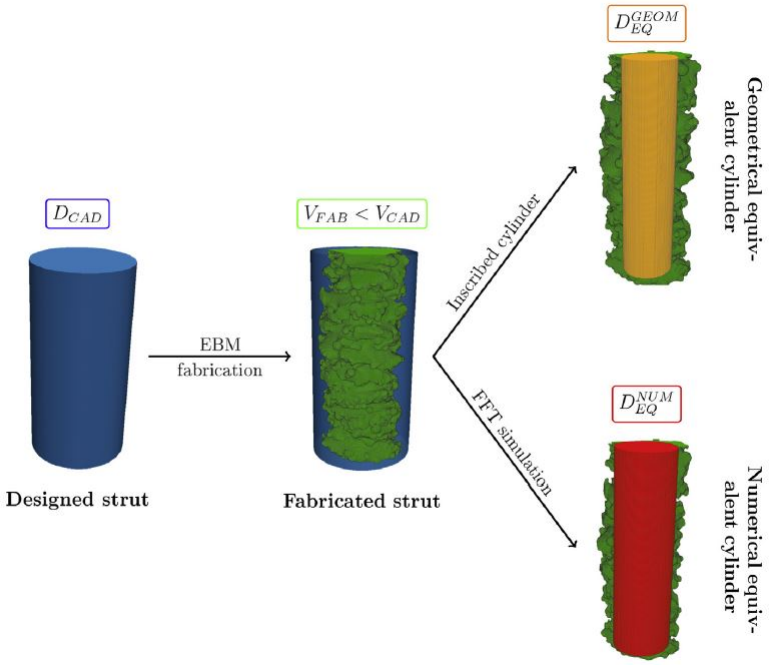

Figure 2.10: Summary of the developed tools for the prediction of the effective stiffness of the struts. A designed strut (blue) is produced by the EBM process. The manufactured strut (green) is smaller than the designed one. Two approaches were investigated. A geometrical (orange) and a numerical (red) equivalent cylinder are extracted to predict the stiffness of the produced strut [3]

When it comes to L-PBF and other powder bed approaches, more should be done to understand the physics behind the layer-by-layer material build-up approach. Thus, it is essential to understand how the process affects the part so that part defects can be anticipated and accounted for when designing the cellular structure or predicting its properties.

2.1.5 Effect of feature quality on feature properties

As stated earlier, surface roughness is essential when it comes to the resulting parts' properties. More info on this is given by the experiment conducted by Qiu [22]. The

experiment consisted of printing AlSi10Mg cellular lattice structures by LPBF. The cellular structures were investigated using optical microscopy and scanning electron microscopy. A compression test was done using a computer-controlled electric screw testing machine under a displacement control rate of 0.2 mm/min. Elements such as strut dimensional inaccuracies and porous structures can affect mechanical properties. Strut dimensional inaccuracies can refer to a difference in diameters between the printed and the designed strut. It can also refer to the misalignment between layers of a strut even if the cross-section of the strut for each layer has the right diameter. According to Qiu's findings, the strut's porosity barely affects the amount of stress within the parts (at least for the quantities that the author investigated). Ideally, more should be done when it comes to exploring how an effective diameter can be used to find the right properties. Mazur et al. performed similar work to describe the lattice structure's properties and the effect that the printing process has on them [23]. Their work was done for various cell types and two-unit cell sizes. Most of Mazur's research compares mechanical properties' differences for the different types of unit cells and unit cell sizes.

Flury et al. tried to evaluate surface roughness's influence on final parts' properties such as surface hardness, elastic modulus, and flexural strength for ceramic materials [24]. They generated a lot of samples to correlate the surface roughness with the cited properties. The samples were divided into six groups with decreasing surface roughness. Different levels of grinding resulted in varying levels of surface roughness. The decrease in surface roughness led to an increase in hardness, elastic modulus, and flexural strength. In the case of hardness, the author stated that the measured hardness was lower for a technical reason: the tip of the hardness indentor gets into contact with elevated parts but not necessarily with lower parts or grooves, which are thus not taken into consideration when doing the test which could result in lower accuracies. Moreover, the indentor's tip did not encounter such problems for the grinded surfaces, which were smoother. When it comes to the correlation between surface roughness and elastic modulus, the same device (same device as the one used to calculate the hardness) was used to calculate the elastic modulus. Therefore, it was also found that the elastic modulus increased as the surface roughness decreased. The authors described how normally, the elastic modulus should not be affected by the increase in surface roughness as the elastic modulus is majorly a property of the whole part and not too much of its surface. Flexural strength was found to increase as the surface roughness decreased, but the author noted no strong correlation.

Although the properties found here may not be affected by surface roughness, other properties can be significantly affected by it, such as heat transfer. In the article written by Seepersad et al. [25], lattice structures have revealed to be promising in areas like heat

transfer. The level of surface roughness of a part can significantly affect the flow of the fluid around the struts by adding more turbulence, which is something the designers might want to avoid. Also, surface roughness does not necessarily affect mechanical properties, but porosity does. As illustrated by the Gibson and Ashby equation, the pores will decrease density, which will increase stress concentration factors, especially for thin struts. It is also shown that porosity can greatly affect the vibrational properties. The natural frequency depends on the mass of a structure; pores' existence may decrease the mass and result in a different expected natural frequency.

2.2 Manufacturing constraints in topology optimization

This section will revisit the topology optimization definition and explain it in more detail to adequately discuss manufacturing constraints in topology optimization. The topology optimization method, which will be described here, is gradient-based. As it was discussed earlier, gradient-based methods refer to techniques that rely on the minimization of an objective function c(x), the compliance, expressed as follow:

$$c(x) = U^T K U = \sum_{e=1}^{N} u_e^T k_e u_e = \sum_{e=1}^{N} E e(\rho_e) u_e^T k_s u_e \tag{2.2}$$

where U is the displacement matrix, K is the stiffness matrix, N is the sum of all the elements e,u_e is the displacement of element e, k_e is the stiffness of an element e, which is obtained by multiplying the Young's Modulus of the element e by the stiffness of a theoretical solid element k_s. The Young's Modulus is a function of the density x_e. The compliance minimization is subjected to the following constraints:

$$\begin{aligned} V(x) = &\quad V_{req} \\ F = &\quad KU \\ 0 < &\ \rho_e < 1 \\ e = &\ 1, 2, 3... \end{aligned}$$

where V_{req} is the required volume fraction, ρ_e is element density and F is the force vector.

Sometimes, constraints can be added as additional terms and multiplied by a coefficient in the main objective function, resulting in a weighted sum, or constraints can be added

as additional objective functions. The latter is referred to as multi-objective optimization. Some optimizers can be used to update the design variables such as optimality criteria method (OCM), method of moving asymptotes (MMA), Globally Convergent Method of Moving Asymptotes (GCMMA), Convex Linearization (CONLIN), Sequential Linear Programming, Sequential Quadratic Programming (SQP) and a couple of others. There are also other topology optimization methods, such as the moving morphable components (MMC) and the level set functions. However, this study will be restricted to the use of gradient-based (SIMP and RAMP) methods. Furthermore, filters can be added to modify the densities and/or sensitivities (derivative of objective and constraint functions) to control specific features. More on this will be discussed in the next chapter.

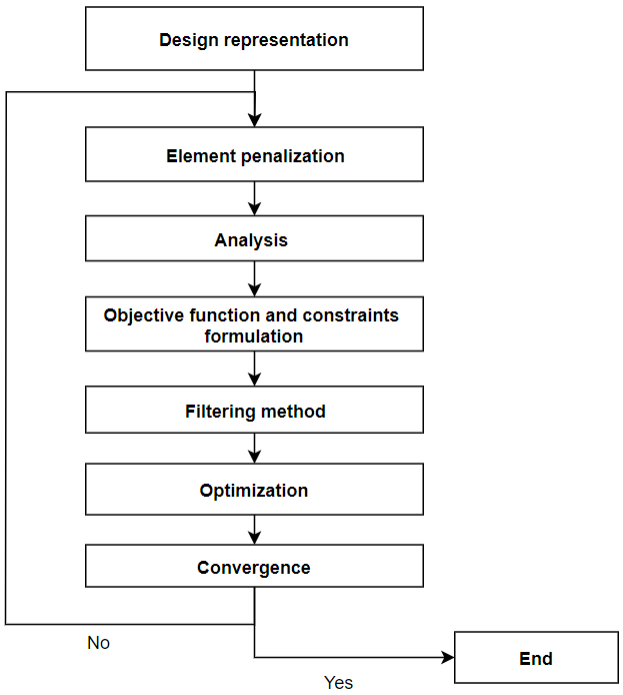

Figure 2.11: Gradient based topology optimization workflow

Using methods like SIMP often results in a gray area representing intermediary values. The resulting structure thus cannot be manufactured. Post-processing technics are needed to ensure a distinction between solid and void elements. One of those technics is Solid Isotropic Microstructure Penalization [26]. The method uses a penalty power to "radicalize" the element density towards 1 (solid) or 0 (void). The formula can be found below:

$$\rho_{e-new} = \rho_{e-old}^{p} \tag{2.3}$$

where p is a penalization factor (usually above 3). Hence the new function to minimize thus becomes:

$$c(\rho) = \sum_{e=1}^{N} \rho_e^p u_e^T k_s u_e \tag{2.4}$$

There is also Rational Approximation of Material Properties (RAMP), which usefulness is to "alleviate the non-concavity" of the SIMP method [27][28].

A few examples have also shown that topology optimization can be achieved through different design representations. The typical way to go about it is through discretization into pixels (2D) or voxels (3D). Still, there have also been some polygonal representations such as moving morphable components or moving morphable voids (MMC or MMV) [8, 29, 30].

A method that has gained popularity during the last decade is the level set method. Osher and Sethian [31] first defined the level set method. It has then been introduced in topology optimization by both Wang et al. [32] and Allaire et al. [33]. A level set curve is defined by the intersection of a plane and of a 3D surface. For each plane or level, the closed curve is described by the function $\phi(x, y)$ x and y being the two coordinates of a point P. The closed curve separates the plane into three regions:

- $\phi(x, y) > 0$ when P is outside the region formed by the closed curve.
- $\phi(x, y) = 0$ when P is on the closed curve
- $\phi(x, y) < 0$ when P is inside the region

The level set curveΓ is thus described the following way:

$$\Gamma = \{(x, y) | \phi(x, y) = 0\} \tag{2.5}$$

As the curve Γ moves in the normal direction with a certain speed v, the level set function is said to satisfy the level set equation:

$$\frac{\partial \phi(x, y)}{\partial t} = v | \bigtriangledown \phi | \tag{2.6}$$

The following equation is also known as the Hamilton-Jacobi, and it can be solved using finite differences.

For many cases, the level set function represents the boundaries of the space containing all possible designs (the design space). Also, the level set method can be used similarly to the Heaviside function as a filtering method. Level set methods can describe the surface's orientation of an object to see where potential manufacturing issues can occur[34]. It can also be used to infer deposition paths from cross-sections of an object [35]. However, more commonly, it can also be used as an optimization method and can easily integrate some common manufacturing constraints [36, 37, 38] as it will be seen in future sections.

There can be as many manufacturing constraints as one can conceive. Constraints can be geometrical (overhang, minimum feature size), or they can be physical (minimizing stress caused by the tools during the manufacturing of the part). This review will focus on some of the geometrical ones.

2.2.1 Minimum feature size

The minimum feature size is a common constraint [39, 8, 40, 41, 42, 43, 44, 45, 46, 47, 48, 30, 49, 50, 51, 52]. The minimum feature size is enforced based on the requirements of the manufacturing tool. As some sizes might not be reached, it is important to enforce a restriction on that parameter.

In order further discuss minimization and maximization methods, it is important to define filtering and projection within manufacturing constraints in topology optimization.

Projection in this context, means transforming continuous inputs into discrete outputs. In a TO context, the inputs are the densities of the elements of a discretized design with continuous volume fractions between 0 and 1 and the outputs are elements with volume fractions equal to 0(void) or 1(solid). Projection is achieved through functions like Heaviside and Sigmoid and it can also be done through level set functions. Examples are given by Sigmund[47] (see fig. 2.12). The filter used by Sigmund is given by the following formula:

$$\frac{\partial c}{\partial x_e} = \frac{1}{x_e \sum_{f=1}^{N} \hat{H}_f x_f} \sum_{f=1}^{N} \hat{H}_f x_f \frac{\partial c}{\partial x_f} \tag{2.7}$$

$$\hat{H}_f = r_{min} - dist(e, f) \tag{2.8}$$
$$\{f \in N |\ dist(e, f) \leq r_{min}, \quad e = 1, .., N\}$$

where $\frac{\partial c}{\partial x_e}$ is the sensitivity, $\hat{H}_f$ is the convolution operator or weight factor.

Filtering means attributing a weight function to an element based on the neighboring elements or nodes; the minimum size gives the number of neighboring elements or nodes

to consider that the user has input. Therefore, the actual density of an element can be rewritten based on the neighboring elements/nodes' density as it is done by Guest [51].

One typical way the minimum feature size is reached is by first filtering and then imposing projection at every iteration. The minimum feature size is imposed during the projection by imposing a distance between the current element and the furthest element that affect the current element.

As it has been discussed earlier, filtering can be done using nodal densities instead of elements densities. The main benefit of using nodal densities instead of element densities is the computational cost. In the case of nodal densities, projection is used to define an element's density based on the densities of the nodes located within a certain radius from that element. For a specific minimum feature size, it is possible to control the number of nodes that have to be considered. However, in the case where elements are used, elements cannot be skipped. This is because there needs to be a density for all of them. Hence, nodal technics might improve the computational cost for specific conditions.

In the case where nodal densities are required, the procedure goes as follows. First, groups of nodes are attributed to each element. Then, for the FEA, instead of only considering the four nodes of the element like it is traditionally done, all the nodes within the "influence zone" of the current element are considered. The stiffness matrix of that element is then built based on the volume fraction of those nodes. The displacement of the element is thus a function of the displacement of those nodes.

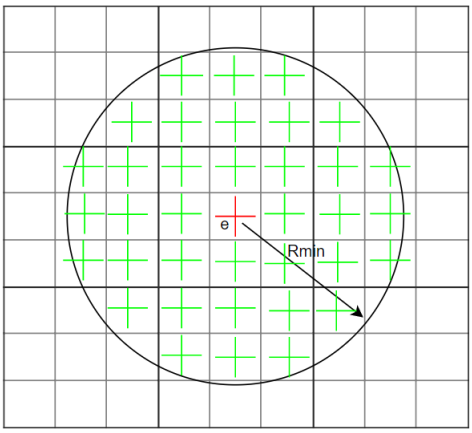

Figure 2.12: Display of elements surrounding e. Those elements are taken into consideration in the filtering of sensitivity for element e.

Zhao et al. [39] have worked on developing viable porous structures that allow the existence of void. The authors map topologically optimized geometries on top of unit cells.

Their TO algorithm used filters to eliminate the need for support structures and impose a minimum feature size. Their algorithm's particularity is that the elements' densities are referred to as the unit cell volume fraction: when the cell becomes smaller, the volume fraction becomes greater. Qian et al. [53] have used the Helmholtz partial differential equation (PDE) to impose a minimum feature size. Gardan et al. [40] designed an optimization workflow to ensure that the parts were adequately printed. They derived a set of guidelines to couple TO with AM.

Lazarov et al. [41] came up with a bandpass filter to restrict the appearance of too thick or too thin elements. They borrowed concepts from dynamics. They used bandpass filters, normally used for frequency limiting, to limit the density of the elements. Mhapsekar et al. [42] gave more of a set of guidelines to minimize the number of thin features, the support structures, and thus the overhangs. They also used a density filter to reduce the thin features, and they used a weighted multi-objective approach to minimize the number of support structures.

Zhou et al. [43] used the weights of other elements to obtain a filtered density. Then, they used the Heaviside function to have a sharp difference between solid and void elements and avoiding gradient zones.

Liu et al. [44] discussed the implementation of minimum feature size for multi-scale topology optimization. In their words, multi-scale TO is "an adaptation of the homogenization-based topology optimization technique to design the local micro or mesoscale structural details of a part or without concurrently optimizing the macro-scale structural geometry". To determine how unit cells would behave, they experimented and concluded that the unit cell size should be selected to be considerably smaller than the part to ensure the homogenization based simulation's accuracy. However, at the same time, it should be larger than the minimum length scale limit to reduce the impact of the length scale constraint.

Osanov and Guest [45] have adjusted the Heaviside projection function to better consider the nature of the layer per layer process. They transformed the space of influence of neighborhood elements/nodes from a sphere to a cylinder.

Vatanabe et al. [46] have studied the effect of a few manufacturing constraints on the final compliance of the optimized part. The constraints they've considered are the minimum member size and the minimum hole size, symmetry, the extrusion, the turning, pattern repetition, forging, and casting. The approach they developed is unified and heavily based on projections, and it can also include additional constraints.

Guest et al. developed a projection method incorporating the nodal volume fractions instead of using the elements' volume fraction [51], the nodes volume fractions are then

projected back onto the element's centroid. Then, the Heaviside projection is used to filter the elements.

One of the topology optimization frameworks, which was developed to ensure a minimum feature size constraint, is the moving morphable components (MMC) found in Zhang's article [30]. A similar method is called "moving morphable voids"(MMV). The MMC method first treats the design space as a set of components or geometrical features that can be parameterized and moved and/or morphed. Trapezoidal components can be defined by six parameters:

$$D = \{x_{11}, x_{12}, x_{21}, x_{22}, w_1, w_2\} \tag{2.9}$$

where $x_{11}, x_{12}, x_{21}, x_{22}$ are coordinates of the endpoints, and the two half-widths w_1, w_2. In order to satisfy the minimum length/size constraint, restrictions are applied on the minimum size, as well as minimum intersection between two components.

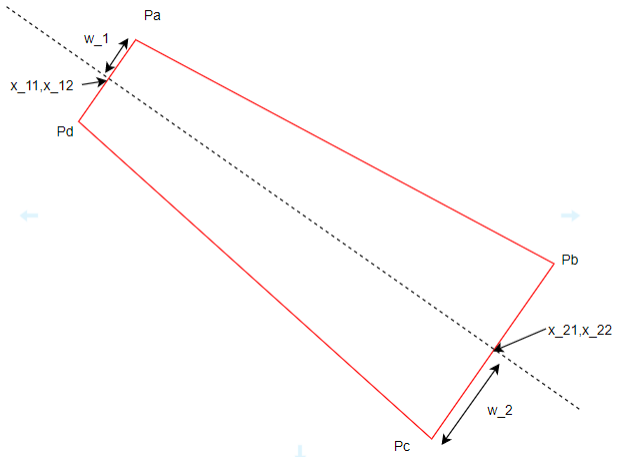

Figure 2.13: Representation of a trapezoidal component with its parameters for MMC

Components are described as trapezoids, which can be seen in figure 2.13. The whole problem can be summarized as follow.

Find:

$$\begin{aligned} D &= ((D^1)^T, ..., (D^{nc})^T) \\ \text{Minimize} \quad I &= I(D, u) \end{aligned} \tag{2.10}$$

Such that:

$$\int_D H(\chi^s)E^s : \varepsilon(u) : \varepsilon(v)dV = \int_D H(\chi^s)f \cdot vdV + \int_D t \cdot vdS, \forall v \in \mathcal{U}_{ad} \tag{2.11}$$

$$\begin{gathered} \mathcal{H}_{\underline{d}}(d_1^{min}, ..., d_{np}^{min}) \leq \varepsilon \\ D \subset \mathcal{U}_d \\ u = \overline{u}, \quad on \quad \Gamma_u \end{gathered}$$

The constraints which takes care of the size is the following:

$$\begin{gathered} V = \int_D H(\chi^s)dV \leq \overline{V}, \\ \mathcal{H}_{\underline{d}}(d_1^{min}, ..., d_{np}^{min}) \leq \varepsilon \\ 2w^{1k} \geq \underline{d}, \quad 2w^{2k} \geq \underline{d}, l^k > \underline{d}, k = 1, ..., nc \end{gathered}$$

2.2.2 Overhang restriction

Overhang restriction is another important constraint, especially with technology such as additive manufacturing(AM). In AM, there needs to be enough material to act as a support for successive layers to be printed. If there are regions with unsupported material (overhangs), removable supports will be added. However, this procedure adds material, takes more time, and also requires supports to be removed, which then requires additional polishing or other post-processing methods. Hence, it is important to minimize the need for support structures, especially the internal ones. Plenty of researchers have worked on this topic [34, 54, 4, 55, 56, 35, 57, 29, 58, 59, 60, 61, 62, 63, 64, 65, 66, 53, 67, 68, 69, 37, 70, 71]

There are a couple of ways the overhang constraints can be dealt with. The first way is through the usual SIMP method. Wang et al.'s [4] have created a constraint using the element(pixels) density. Any pixel with not enough pixels under it is penalized. The function is described in the following way.

$$\begin{aligned} o_{i,j} &= 1 \quad for \quad x_{\Delta i,j} > 0 \\ o_{i,j} &= 0 \quad for \quad x_{\Delta i,j} \leq 0 \\ x_{\Delta i,j} &= x_{i,j} - (x_{i-1,j-1} + x_{i-1,j} + x_{i-1,j+1}) \end{aligned} \tag{2.12}$$

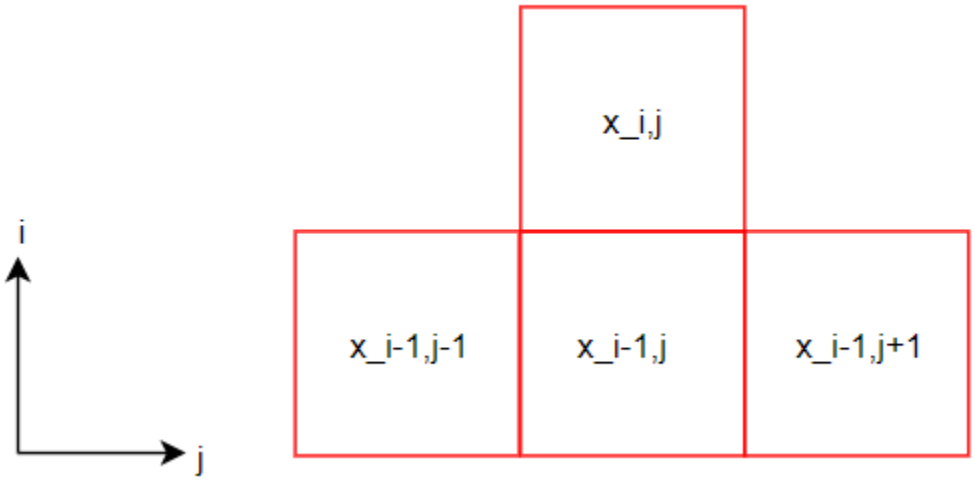

Figure 2.14: Pixels indexing in Wang et al.[4]

where $x_{i,j}$ is the density of the element with coordinates i and j. Satisfying the original conditions is usually done through a specific function (see fig. 2.14). Many articles use the Heaviside density projection or versions of it [54, 45, 53, 55, 72].

For MMC, the same definitions are reused from the previous section however the constraints are changed. Instead of the size constraints, the overhang constraints are defined the following way:

$$V = \int_D H(\chi^s) dV \leq \overline{V} meas(D), \tag{2.13}$$

$$(sin(\theta_k + \alpha))^2 \geq (sin(\overline{\theta})^2, k = 1, .., nc \tag{2.14}$$

$$0 \leq \underline{\alpha} \leq \alpha \leq \overline{\alpha} \leq \pi/2 \tag{2.15}$$

Cacace et al. [34] have used a level set method to represent the shape for which they want to eliminate the overhangs. Using level sets allows them to find the normal at all the surface points and add material to it until there are no overhangs. The main drawback of this method is that it is all done after the topology optimization process. There is no coupling between the minimization of compliance and the elimination of support structures; the final part might not be the most optimal.

Fortunately, some methods try to eliminate the overhangs while optimizing the part.

Garaigordobil et al. [54] developed a method called "Smallest Univalue Segment Assimilating Nucleus" (SUSAN). The method detects the edge through masks (3x3 pixels arrays), which allows them to obtain the density gradient for all positions within the design space. The overhang constraint is derived based on the sum of the values obtained from the masks.

Jankovics et al. [56] have developed a code in which they defined what is called a surface area sensitivity where they calculate the surface area of each element with respect to its density. The surface area sensitivities are added to the compliance sensitivities to obtain a final result.

Liu et al. [35] incorporated deposition path planning in topology optimization to address the anisotropy problem during the printing. In their case, multi-level sets are used to represent the different layers. They used this principle to ensure the layers are self-supported as well and to ensure that the model resembles the final printed part.

Gaynor and Guest [57] have developed a procedure to impose a minimum length scale and a minimum inclination. This was all done using projection. When it came to the inclination restriction, they only considered the nodes around the specific element below a certain angle.

Guo et al. [29] have also used the MMC method to achieve a minimum inclination for optimized structures.

Langelaar et al. [61] have defined a filter in which they used both a blueprint density (the original density given by the optimization) and a printed density. The printed density is the minimum between an element's blueprint density and the maximum printed density of the support elements. They used an approximation function to take the derivatives for the printed density of each element. The approximation is used to modify the sensitivities in a filter.

Li et al. [62] have developed a way to constrain low inclined surfaces and avoid unprintable circles by converting them into ellipses. In their case, the procedure is applied after the optimization.

Mass and Amir restricted the minimum angle using truss optimization [63]. Their procedure works as follows: a ground structure within the design space is optimized with a minimum angle restriction for all the struts. The resulting optimal truss is used as a skeleton upon which they create the continuum structure (based on FE). Only certain elements located at a certain distance from the skeleton are considered.

Leary et al. [65] also came up with a method to construct the lines after the optimization process, they first smoothed the boundary, then measured the local gradient and identify

the infeasible domains. They have built internal boundaries by generating lines starting from the points going downwards at a specific angle.

Thore et al. [66] have opted for a penalty regulation to control their overhanging features. They have based themselves on Langelaar's approach and added weight factors to penalize sharp corners.

Mirzendehdel et al. [67] analyzed how the support structures were generated in the first place. They defined the support structures as the integral of the support length over the boundary multiplied by a filling ratio. In the objective and constraint formulation, they expressed the support structures as a constraint, and they then try to bound the constraint. Hence their set up reduces the need for support structures but does not eliminate it.

Johnson and Gaynor have extended Gaynor's approach to 3D [68].

Zhang et al. [37] opted for the modification of holes in the optimized shape (treating holes as polygons). The method is similar to the MMC/MMV.

Zhang et al. [69] proposed a methodology to "sprinkle" overhang features with upside-down triangles which respect the minimum angle.

Van de Ven et al. [70] created a filter that eliminates overhang zones. They achieve this using a continuous front propagation to study the progression of the edges.

To develop a constraint that ought to alter topologically optimized structures, it is important first to determine the critical geometrical features by evaluating the performance of all features.

Chapter 3

Impact of the minimum-feature-size and overhanging angle on the surface quality of the final AM part: Qualitative study

This research aims to understand how certain geometric parameters affect the surface quality of a design feature. Selecting prisms as design features reduce the geometric parameters to three: length, orientation, and thickness. The next step is to understand the importance of those geometric features. There are a couple of articles that have done similar work [8, 23].

An experiment was modeled after the ones done by the cited authors[8, 23]. However, for simplicity reasons, the length parameter was neglected. From observations made in experiments from the literature, the surface roughness of downfacing surfaces does not increase uniformly over the whole length. Therefore, a surface roughness value for a specific length would not be explicative of what is truly going on. For example, when considering two struts that both have fixed angle θ_i and fixed thickness r_{min}, the surface roughness of the strut with the bigger length is an accumulation of all the surface roughness values of the struts with smaller lengths. The accumulative effect might influence the conclusion from the results; hence, the length has been dismissed as a parameter for the current study.

The purpose of the experiment described in this chapter is to analyze the selected design features' surface quality. The design features were the oriented struts, and the surface quality alludes to the surface roughness of the struts' bottom surface.

Although the experiments will give information on the final result's surface quality, experiments are often expensive to make. Therefore, it can be an opportunity to develop

and test a model to predict the surface quality of a feature.

3.1 Prediction of the design constraints' impact

When it comes to LPBF and other powder bed approaches, more should be done to understand the physics behind the layer-by-layer material build-up approach. It is thus important to understand how the process affects the part so that part defects can be anticipated and accounted for when designing any structure with those features.

The parameters which can affect features can be divided into two parts: the geometrical parameters and the process parameters. In this work, printability refers to three things: dimensional fidelity, low surface roughness, and low porosity. It is important to have a firm understanding of those elements to determine how the mechanical properties, among others, will be affected. The following section will review how each of the parameters may affect the manufacturability of the structure.

3.1.1 Effect of layer thickness

Layer thickness is a process parameter that can drastically influence the precision of a part. For parts with high variation in curvature along the z-direction (with respect to the build plate and the chosen orientation of the part), it is advised to use thinner layers. A few papers have worked on optimizing the procedure for slicing software such as the paper from Sikder [73]. However, this often requires adapting the layer thicknesses based on the detail of a particular feature, which can be done for extrusion processes. However, this cannot be done for powder bed processes because powder bed systems involve a recoater which spreads powder evenly across the platform. Overall, the thicker the layer is set to, the higher the surface roughness. However, this also depends on the orientation of the design feature. The design feature in this particular case is the strut. For vertical struts, the surface roughness, the layer thickness will not significantly affect their surface roughness as much as it will affect the surface roughness of oriented struts. A model for the strut can easily be developed to showcase the effect of the strut's orientation on the surface roughness. The model is shown in figure 3.1, along with the parameters necessary to describe the surface roughness.

The paper by Strano et al. gives an adequate example of how surface roughness influences the lattice properties [15]. They analyzed surface roughness of different parts in

their work, and they then used a model to predict surface roughness in selective laser melting. The surface was characterized at different angles using a scanning electron microscopy. However, the experimental data did not match the model, which was proposed. The main problem with such a model is that it does not take into consideration the fact that the particles attach themselves to the surface: for smaller orientation, the width of the steps is bigger than the powder particles size, whereas, for higher angles, the steps' width come close to the actual size of the particles. This phenomenon is also highlighted in Calignano's paper [74]. The author explains how the surface roughness comes (partially) from the additional, partially melted powder particles which have stuck to the part. Those additional powder particles are more recurrent for overhang surfaces. This is because the heat flows toward the bottom to create the melt pool. Since the strut has been sliced, it consists of a bunch of stacked up flat cylinders. To consider such a phenomenon, Strano et al. established that a random portion of the step will have particles stuck to it. The present work inspires from itself from the work of Strano et al. A thickness λ represents the portion of added particles added to the downfacing surface.

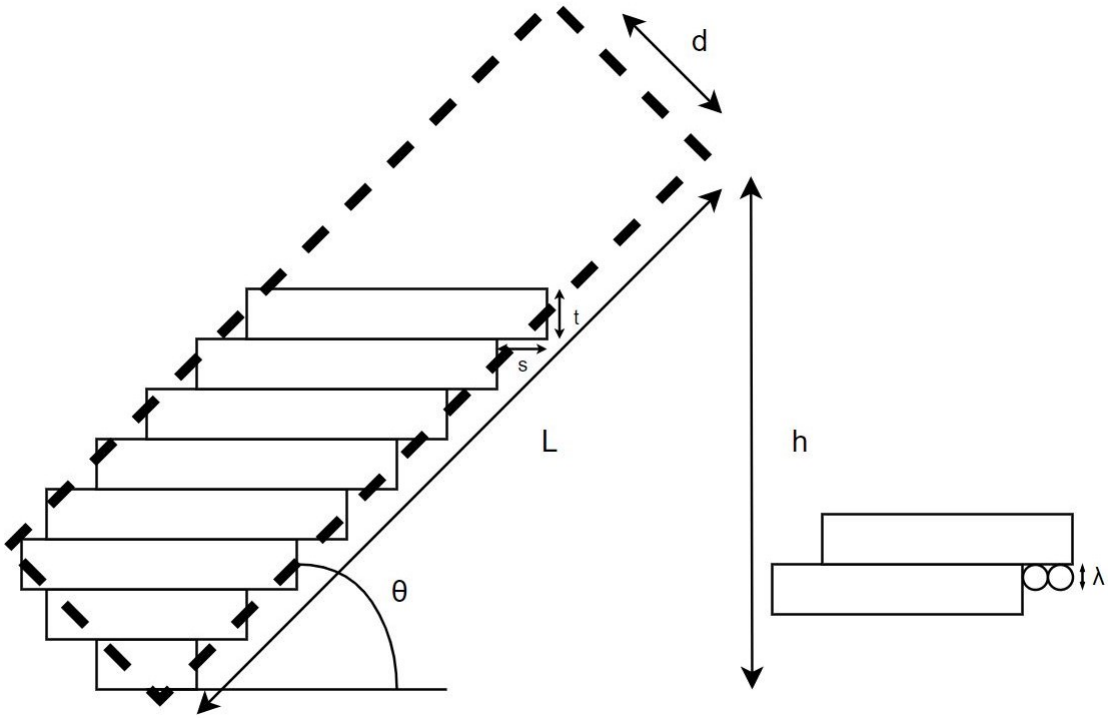

Figure 3.1: Diagram showing the layers in a printed strut

Only the two-dimensional profile of the strut has been taken. L refers to the length of the strut. The width (or diameter) is described as w. The height of the strut is h. Theta

refers to the strut's angle with respect to the x-y plane, t refers to the thickness of one layer, n refers to the number of layers. The number of layers for a strut is given by dividing the height h by the layer's thickness. The height of the strut is defined by the following formula:

$$h = L \cdot sin\theta + w \cdot sin(90 - \theta) \tag{3.1}$$

The last term describes the exterior of the strut's external portion that is often connected to other struts. Therefore the height of the strut can be simplified to :

$$h = L \cdot sin\theta \tag{3.2}$$

Using the number of layers and the space between layers (s), it is possible to obtain the final theoretical surface roughness (SR).

$$n = \frac{h}{t} \tag{3.3}$$

$$s = tan(90 - \theta) \cdot t \tag{3.4}$$

Since the overhang angle is taken from the line normal to the build plate, the angle is subtracted from the 90 degrees. The result can be seen below:

$$SR = n \cdot \frac{s/2 \cdot t/2}{2} + n \cdot \lambda \cdot s \tag{3.5}$$

$$SR = \frac{L \cdot cos(90 - \theta) \cdot (8 \cdot \lambda + t)}{8} \tag{3.6}$$

When it comes to porosity based on the strut orientation, many things need to be considered: Delroisse et al. studied the effect of inclination on struts' porosity. The experiment they have done was mainly applied for AlSi10Mg [5]. Their study used two different inclinations, one vertical strut and one oriented strut. The analyzed struts were part of a larger lattice structure to avoid the effect of free borders. All of the cross-sections (cross-section were taken on planes parallel to the X-Y plane) were investigated, and they found that the vertical struts were much more homogeneous than the inclined strut; the inclined strut was more porous. They found that the reason for such a discrepancy lies in how the heat of each layer flows through the existing part of the strut. For oriented struts, there are two different zones. The first one is the lower part of the strut, which results from the heat going through previously unmelted powder (cooling takes more time), and the

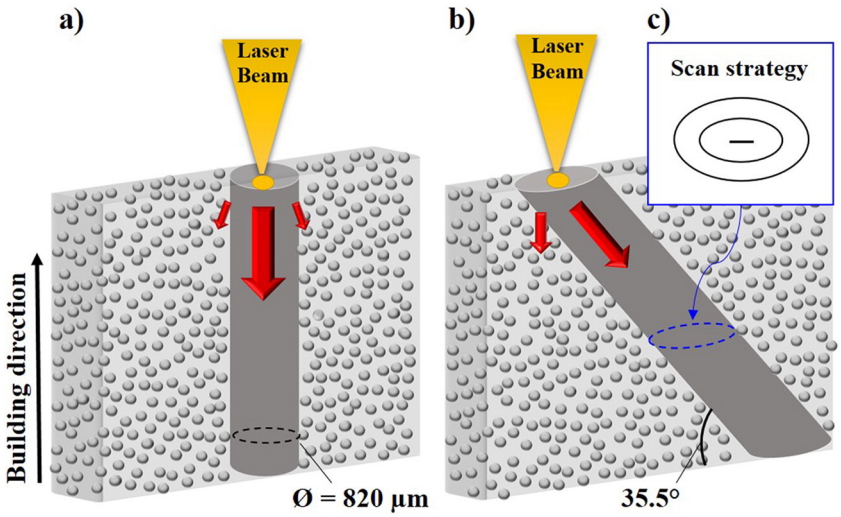

Figure 3.2: Diagram of (a) the vertical, (b) the inclined struts and (c) the scan strategy. The red arrows indicate the thermal flux density and direction [5]

second zone describing heat going through previously melted powder. The two zones can thus only be present within the inclined struts. The existence of those two different zones created by the difference in cooling is seen through the microstructure of the shape, and it also influences the hardness of measurements on the two different struts. The porosity also differs quite a bit because between the two zones in the inclined struts. A rigorous mathematical model to approximate the porosity based on the strut angle and diameter can thus be developed as it is done in figures 3.2 and 3.3.

3.1.2 Effect of laser properties

When fabricating CM via LPBF, driving parameters are the laser beam power and laser scanning speed. Qiu et al. [22] review the effect of these print parameters on fabricating diamond AlSi10Mg structures. The research group found that within the bounds of their process window, the struts' diameter, the surface roughness, and the porosity increased as the laser power increased. Besides, the porosity was greater for intermediate laser scanning speed (3000 mm/s - 5000 mm/s). These two observations are corroborated in other works [75, 76, 77] as well for LPBF. To better understand how those parameters affect the part, it is important to understand the melt pool behavior transitioning from conduction to stable and unstable keyhole mode. In conduction mode, depending on the power level, the melt pool increases in volume, and typically in width resulting in fabricated lattice

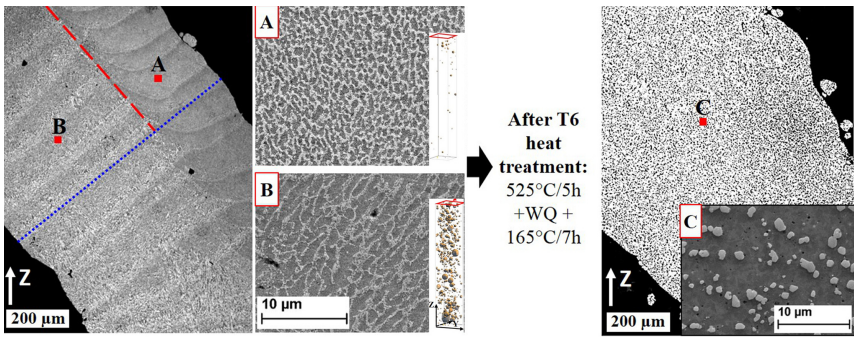

Figure 3.3: Light and SEM(zoom) micrographs of the microstructure in an inclined strut. (a) Upper zone A presents a fine microstructure while lower zone B presents a coarser cellular dendritic microstructure. The blue dotted line is the cut plane for Fig. 3.2. (b) Homogenized microstructure after a T6 heat treatment (525°/5 h + water quenching (WQ) + 165°/7 h) [5]

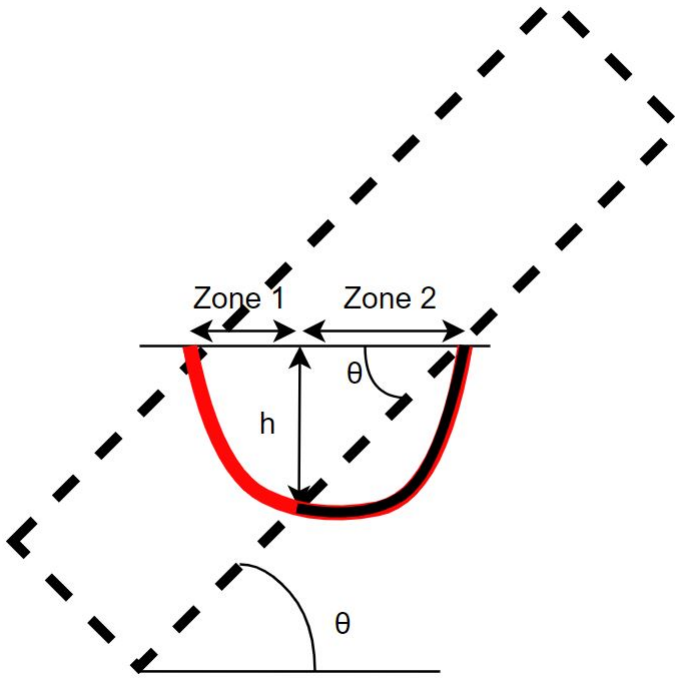

Figure 3.4: Diagram of a strut's porous zones

structures' features becoming larger than the primitive design features. When increasing the power input further and transitioning into a stable keyhole, the melt pool narrows and deepens; thus, the surface quality may increase, and porosities can be reduced due to the re-melting of underlying pores [78]. When increasing the power level even further, the process can quickly transition into an unstable keyhole. Material vaporization and material spattering can cause melt pool flow instabilities, causing porosities to occur and poor surface quality[79].

Many researchers have explored the effects of process parameters on lattice structures. Liu et al. [80] used a bi-pyramidal unit cell and investigated the effects of the different parameters on the feature qualities of the final product. The study was conducted using Titanium alloy via LPBF and investigated the effect of laser scanning speed and laser power. The authors found an increase in porosity, which they attributed to the vaporization of the alloy elements.

Sing et al. [81] found that, for commercially pure titanium fabricated via LPBF, manufactured struts' diameters were smaller than what they were designed as primitives. The struts also had sizable powder adhesion. Through ANOVA (analysis of variance), it was found that laser power and scan speed have a significant effect on powder adhesion. Only the geometry of the cells and the struts' diameters affect the elastic constant of the lattice. Qiu et al. performed a study to understand better the influence of processing conditions on strut structure [22]. The test was done on periodic bi-pyramidal unit cells. They found that the struts' diameter deviated from the design and that the diameter was increasing the laser power monotonically, that the laser power led to an increased molten pool width and, consequently, an increase in the struts' diameter. Porosity is larger for intermediate powers.

Qiu et al. established the role of melt flow to the increase in surface roughness [82]. They have linked melt flow with surface roughness. They claimed that unstable melt flow is responsible for an increase in porosity and surface roughness. According to them, the melt flow instability phenomenon is the Marangoni force (thermo-capillary force) and recoil pressure. High laser power and low powder layer thickness help to reduce the melt flow and thus the porosity. Whereas increasing layer thickness increases the porosity levels.

3.2 Design of experiment

The work by Mazur et al. [23] heavily influenced the design of the experiment.

3.2.1 Methods

This experiment aimed to correlate the design features (orientation and thicknesses) to their printability for the Hastelloy material. To do so, two batches of ten samples were printed: ten solid struts and ten hollow struts. Each of the samples was constituted of nine struts with radii ranging from 0.1 to 0.9mm with a 0.1 mm increment for solid struts and with inner radii ranging from 0.1 to 0.9mm with a 0.1 mm increment and outer radii ranging from 0.3 to 1.1 mm with a 0.1 mm increments for hollow struts. Each sample of the batch had a different orientation ranging from 0° to 90° with 10° increment. The strut's length was 8 mm. Six other structures were constructed based on lattice structures (lattice cubes). Using three different unit cells and two different thicknesses (0.2 mm diameter and 0.6 mm diameter), as seen in figure 3.9. The main motivation behind hollow struts is the advent of embedded sensors in AM parts [83]. In fact, due to AM parts' unique characteristics, the sensors can be embedded directly into parts enabling the full mechanical, thermal, and other properties to be known at all the structure's locations through tests.

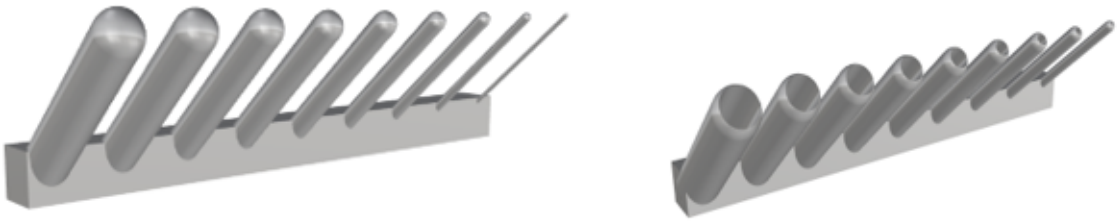

Figure 3.5: Visuals of the solid and hollow struts printed for this experiment

3.2.2 Equipment

Printing parameters

The samples were printed using the EOS M-290 machine in the MSAM lab. The material used was Hastelloy. For the lattice cubes, the hatch distance used was 0.07 mm, the scanning speed was 1750 mm/s, the power used was 115W, and the beam offset was 0.005mm. For the batches of single struts, the hatch distance used was 0.09 mm, the scanning speed was 1250 mm/s, the power used was 155W, and the beam offset was 0.015mm.

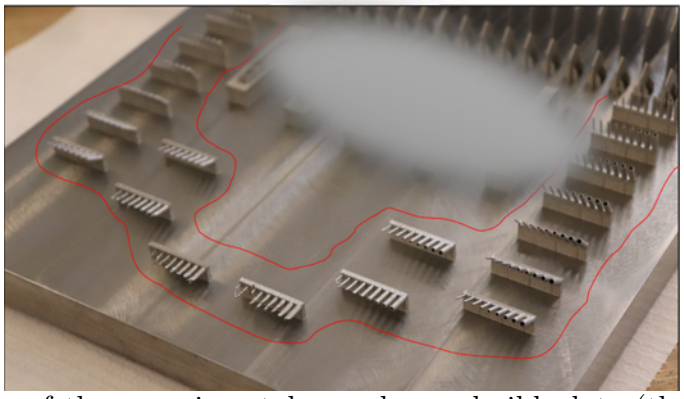

Figure 3.6: Diagram of the experimental samples on build plate (the builds blocked are part of another experiment)

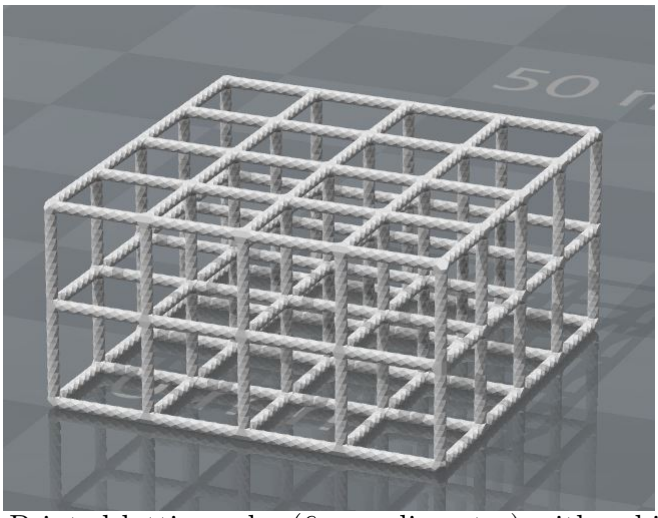

Figure 3.7: Printed lattice cube (6 mm diameter) with cubic unit cells

Microscope

Samples were analyzed using the laser scanning confocal microscope from Keyence with a 10x magnification range. For all the differently oriented sets, only the larger struts in each inclination were printed.

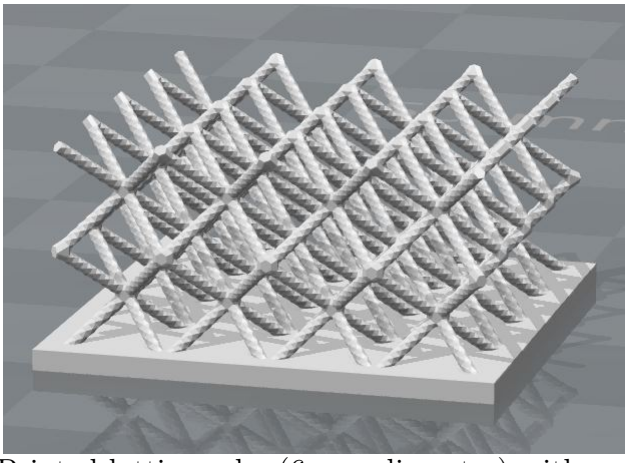

Figure 3.8: Printed lattice cube (6 mm diameter) with cross unit cells

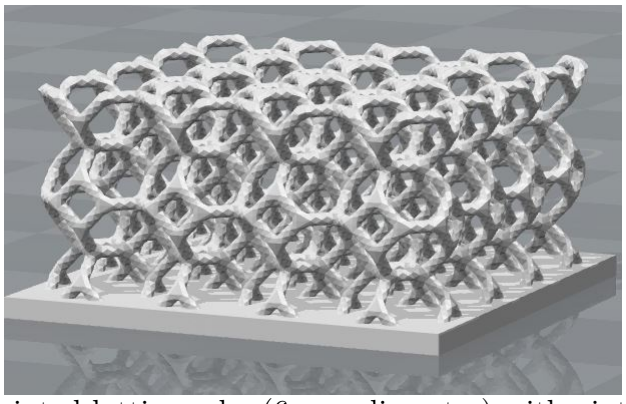

Figure 3.9: Printed lattice cube (6 mm diameter) with vintiles unit cells

3.3 Results and discussion

3.3.1 Surface roughness

Surface roughness was measured for the thickest strut of each orientation. There have been many problems in estimating the surface roughness; in part, it was due to the struts' cylindrical shape. To estimate the surface roughness, only a thin line was considered on top of the strut's downfacing part. However, the results still varied depending on the location of the strut on which the lens focused. Therefore, multiple locations were chosen and averaged out. The other problem was the sample size: the sample often collided with the lens and made it hard to conduct the experiment. Despite all of this, the surface roughness obtained in table 3.1 agrees with some of the predictions made in equations 3.5. For low angles, the surface roughness was higher, and for high angles, the surface roughness

was lower. As the angle increases, the roughness drastically decreases and then does not change a lot. The main difference between the two types of predictions and the results is the trend. The difference in trend can be seen in figure 3.10. The actual predictions results were scaled to match the ones of the experiment. Arbitrary values of L =10, lambda =10, and t = 8 were chosen for the scaling up. The results for both types of struts are not very conclusive since there is not a particular trend to obtain from either of them.

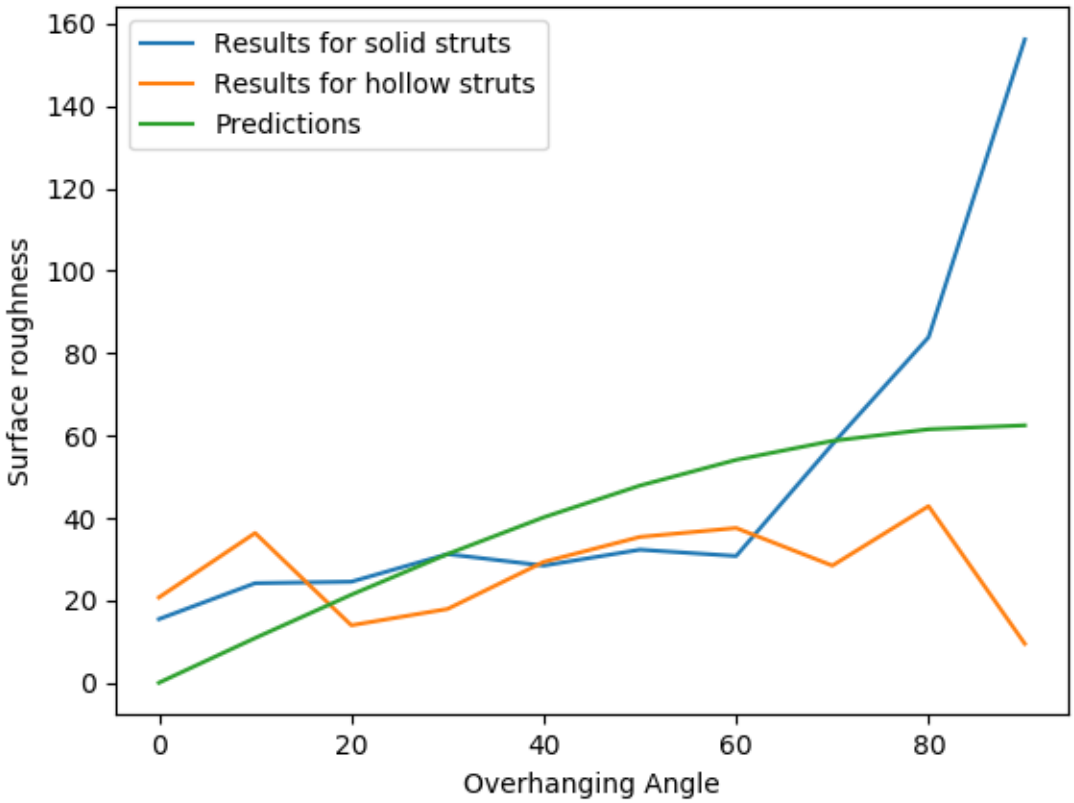

Figure 3.10: Predictions' trend against actual results

The behavior is the same for both hollow and solid struts. To better qualify the build quality of design features, tables of scores were obtained using a specific index. The results obtained can be summarized in the tables 3.2 and 3.3. Each entry has a score that ranges from 0 to 6. 0 refers to viable build quality (maximum), and 6 refers to the worst surface qualities. To come up with a score, numbers were added depending on specific criteria:

Table 3.1: Surface roughness (μm) of thickest strut for each orientation

	Outer Diameters	0.9	1.1
	Inner Diameters	0	0.9
Angle	90	156.21	9.46
	80	83.91	42.885
	70	57.89	28.445
	60	30.77	37.57
	50	32.305	35.41
	40	28.45	29.35
	30	31.225	17.91
	20	24.525	13.95
	10	24.17	36.35
	0	15.45	20.71

- If the down-facing part of the strut had a low visible surface roughness or if the part was slightly bent, a 1 was added.
- If the strut's length had been changed (reduced), a 2 was given.
- If there was a highly visible surface roughness or most of the surface was deformed, a 3 was given.

The final score is the addition of all of those. When the strut was removed, the entry was given as NA (not applicable). NA- B refers to struts that were partially removed and bent. There are a few common trends that validate the predictions made earlier. As can be seen, a lot of the struts have been removed, especially for the thinnest. This is due to their sensitivity and the low cross-section area. It is harder to pile up layers when the area is small. Then, the struts with inferior build quality (high surface roughness) are the ones with the largest overhang angle, which confirms the theoretical predictions. Then colors were given on the entry based on the score - green represents a score of 0, yellow is for a score of 1 or 2, orange is for a score of 3 or 4, and red represents the rest of the cases (NA, 5 or 6).

There are a couple of differences between hollow and solid struts. The main difference between the hollow and solid struts is that the thinnest hollow strut was thicker than the thinnest solid strut. This contributed to the increasing in the build quality of the hollow struts. The hollow struts show an exciting way of working with lattice. As the strut can be lightweight while keeping diameters above the minimum printable diameter.

	R_o	0.1	0.2	0.3	0.4	0.5	0.6	0.7	0.8	0.9
Angle	90									
	80									
	70									
	60									
	50									
	40									
	30									
	20									
	10									
	0									

Table 3.2: Qualitative assessment of solid struts

Contrarily to the predictions, when considering only the overhanging angles, the tables show that the features are printable below a certain overhanging angle. According to the prediction, the transition from low to high quality for different radius values should not all take place at the same overhang angle. However, it is important that the two tables only analyze the quality qualitatively.

Amongst all the lattice cubes, only the thick cubes with the "vintiles" based unit cells and "cross" based unit cells survived, mostly because they had no vertical strut and also because they were thick. Lattice cubes with thin struts failed. However, the thick lattice cube with the "cubic" unit cells failed due to the orientation of its member; it was due to the number of overhangs. As it can be seen in figure 3.9, the lattice cubes with cubic unit cells have a lot more horizontal struts than the lattice cubes based on other types of unit cells.

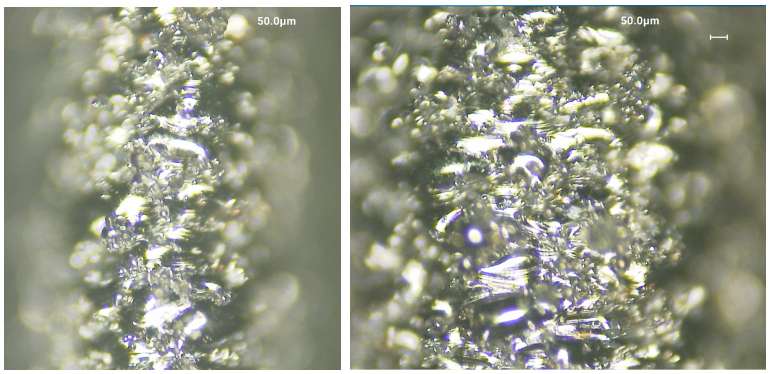

Figure 3.11: Images of the downfacing surfaces of two vertical struts, 0.4 mm diameter (left) and the 0.9 mm diameter(right)

	R_o	0.3	0.4	0.5	0.6	0.7	0.8	0.9	1	1.1
	R_i	0.1	0.2	0.3	0.4	0.5	0.6	0.7	0.8	0.9
Angle	90									
	80									
	70									
	60									
	50									
	40									
	30									
	20									
	10									
	0									

Table 3.3: Qualitative assessment of hollow struts

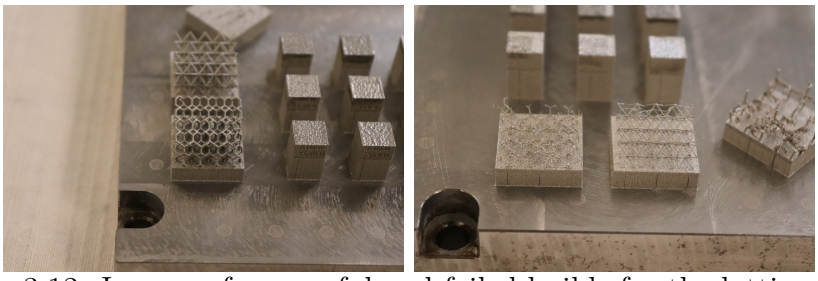

Figure 3.12: Images of successful and failed builds for the lattice cubes

3.3.2 Porosity

Samples were analyzed using the Zeiss Xradia 520 Versa 3D X-ray Nano-CT scanner. Images were analyzed using the Dragonfly software (see 3.13). It was noticed that the porosities are concentrated more towards the bottom surface than towards the upper surface, which contradicts, once again, the predictions. However, it was also found that the porosity itself was smaller than 1%, which was estimated to be "good enough".

Figure 3.13: Top view of the porosity distribution for solid struts of different sizes (30° orientation). Pores are in red

Chapter 4

Impact of the minimum-feature-size and overhanging angle on the surface quality of the final AM part: Quantitative study

4.1 Design of experiment

By observing the previous experiment results, it is clear that there wasn't enough data obtained to describe the build qualities properly. Furthermore, the samples' characterization was qualitative instead of quantitative, which limited the information that could be extracted. Then, the other problem lied in the fact that cylindrical models were used, and it reduced the possibility of detailing the surface quality (the samples could not be properly put on the resting plate of the Keyence microscope). Therefore another experiment had to be done. However, this time, a more quantitative approach is going to be taken. Instead of using a qualitative metric as it was done in the previous experiment, the metric was the surface roughness of the features' downfacing surfaces. To do so, 11 samples, each containing 13 struts, were printed. The struts were square prisms. The side of the square varied from 0.2mm to 0.8mm with a 0.05mm increment. Each sample was printed at a different OA ranging from 20° to 70° with a 5° increment. The strut's length was 10 mm. The idea of square prisms was essential to set up the samples under the Keyence microscope properly.

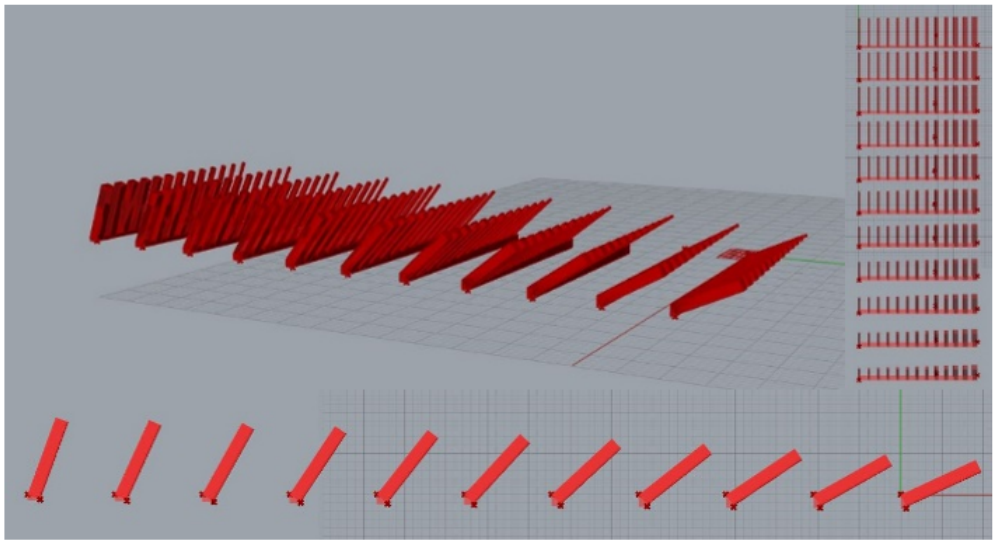

Figure 4.1: Computer-aided-design models of the experimental specimens

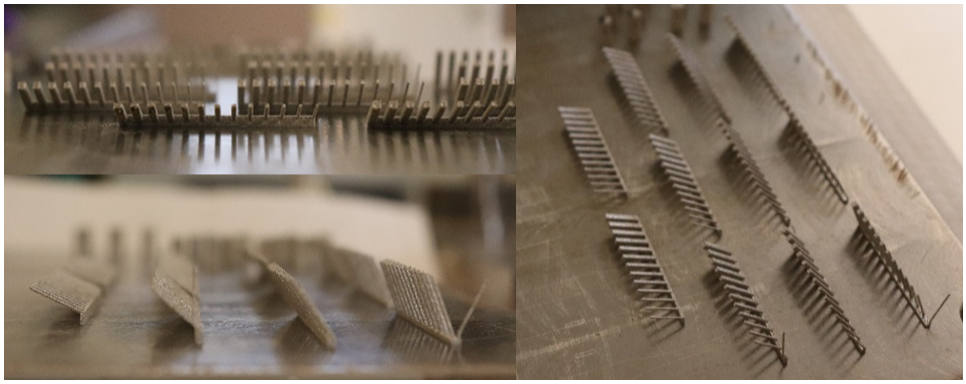

Figure 4.2: Manufactured samples

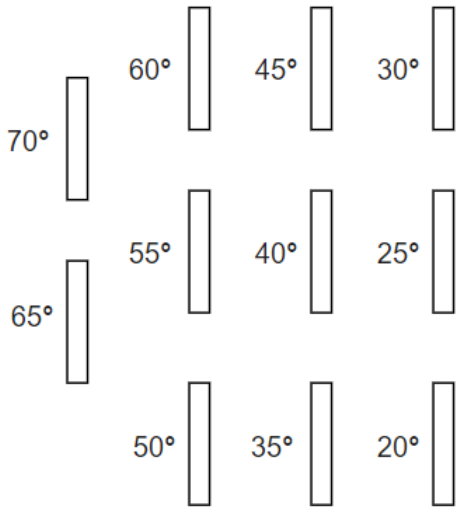

Figure 4.3: Configuration of specimens on the build plate

The samples were printed using the EOS M-290 machine in the MSAM lab. The material used was Hastelloy. For the single struts, the hatch distance used was 0.09 mm, the scanning speed was 1250 mm/s, the power used was 155W, and the beam offset was 0.015mm.

Samples were analyzed using the laser scanning confocal microscope from Keyence with a 20x magnification range. The samples were aligned under the microscope, and 5-6 measurements were taken along the downfacing surfaces for all the samples' features.

4.2 Results and discussion

The final table with the surface roughness based on the orientation and the size of a feature is shown in table 4.1.

Compared to the qualitative tables shown in the previous section, the quantitative table 4.1 allows the viewers to see the gradation in terms of surface qualities. As expected, the features with the highest surface qualities are usually the thickest and most vertical struts and the ones with the lowest surface qualities are the thinnest and horizontal ones. It is important to notice that there have been some measurement errors during the characterization of the down-facing parts of the struts. Those errors can explain some of the irregularities in the table.

	70.00	65.00	60.00	55.00	50.00	45.00	40.00	35.00	30.00	25.00	20.00
0.20	53.99	36.05	34.69	28.03	28.83	36.05	34.71	28.39	24.72	29.83	34.82
0.25	47.31	34.90	32.07	31.94	39.62	32.43	28.82	22.45	20.75	20.06	15.94
0.30	41.02	36.20	29.66	38.60	32.04	19.17	57.38	31.39	18.06	21.51	18.03
0.35	48.81	34.22	31.99	31.80	26.29	30.55	31.49	26.04	22.14	23.48	16.24
0.40	48.50	37.96	33.92	41.56	30.76	26.19	29.40	26.81	17.79	21.42	23.22
0.45	50.18	40.80	35.83	32.29	31.27	25.43	32.87	22.03	19.97	21.03	18.64
0.50	45.11	38.90	36.42	32.70	31.48	24.62	33.00	23.39	18.49	18.82	17.45
0.55	60.72	37.12	33.99	39.02	32.93	25.30	25.98	20.18	18.85	20.35	17.84
0.60	56.33	43.13	35.12	34.48	30.86	24.03	33.23	21.75	19.45	17.58	20.48
0.65	52.82	34.13	33.07	42.66	31.00	25.52	30.65	22.15	19.27	18.08	18.91
0.70	43.82	31.68	34.51	37.56	28.67	28.33	31.24	23.66	18.32	13.95	18.01
0.75	52.05	32.37	32.29	31.94	30.60	30.08	34.48	23.09	19.65	17.61	18.41
0.80	50.78	36.72	34.50	31.97	29.60	25.20	34.63	21.66	18.04	17.62	18.71

Table 4.1: Surface roughness table. The columns represent the overhanging angles in degrees while the lines represent the radii in mm

For visualization purposes, the table was turned into a 3D surface. A surface point had three coordinates, the first two coordinates are the OA and the thickness, and the last coordinate, or the height, is the surface roughness (see figure 4.4).

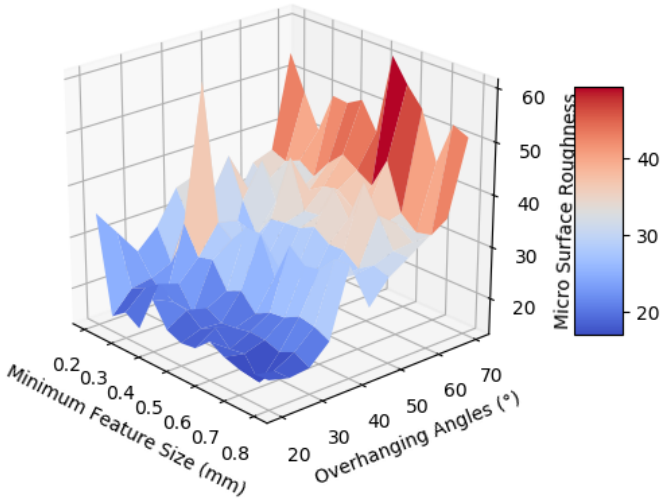

Figure 4.4: Data from Table 4.1 plotted as a surface

During the last experiment, only the thickest struts' surface roughness had been measured for all overhanging angles. In the present experiment, surface roughness measurements have been obtained for each orientation's different thicknesses. It is thus an occasion to investigate how the theoretical predictions from experiment 1 hold. To do so, the same equation 3.5 was plotted against the surface roughness associated with each overhanging angle for each thickness (figures 4.5 to 4.17). The equation's parameter t of the equation was multiplied by a coefficient that ranged from 0 to 1 based on the maximum thickness.

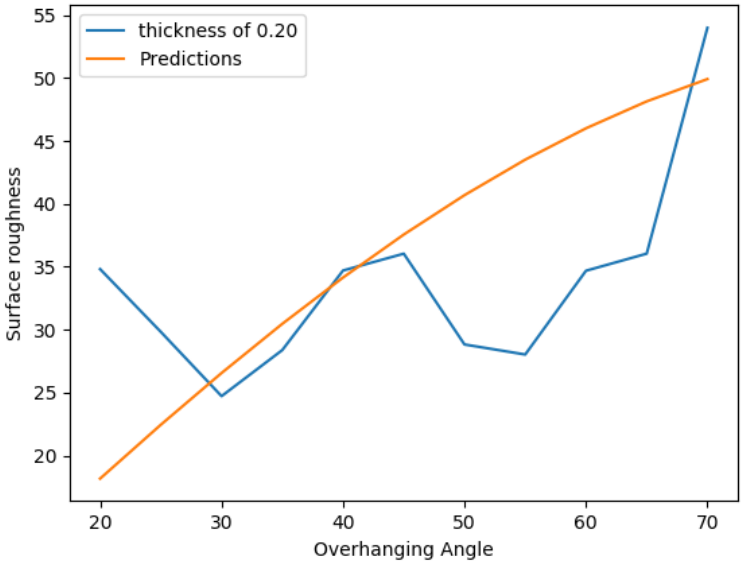

Figure 4.5: Overhanging angle plotted against the surface roughness of down-facing surfaces for a thickness of 0.2 - experimental results in blue, predictions in orange

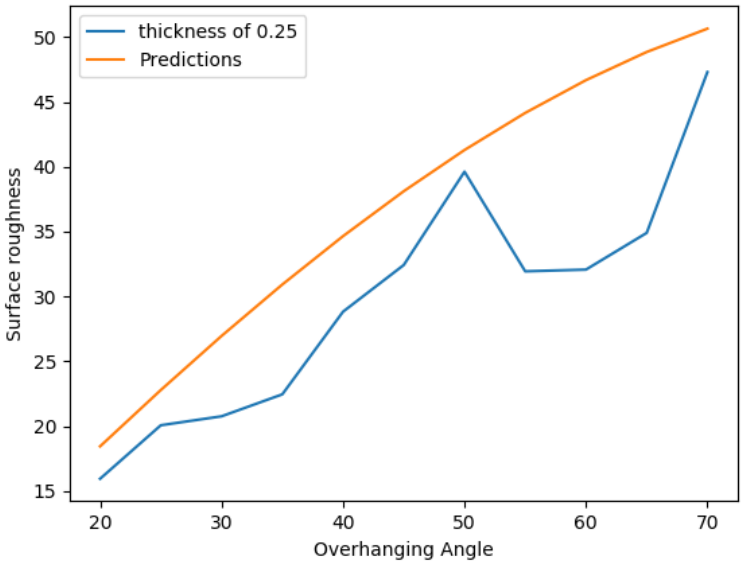

Figure 4.6: Overhanging angle plotted against the surface roughness of down-facing surfaces for a thickness of 0.25 - experimental results in blue, predictions in orange

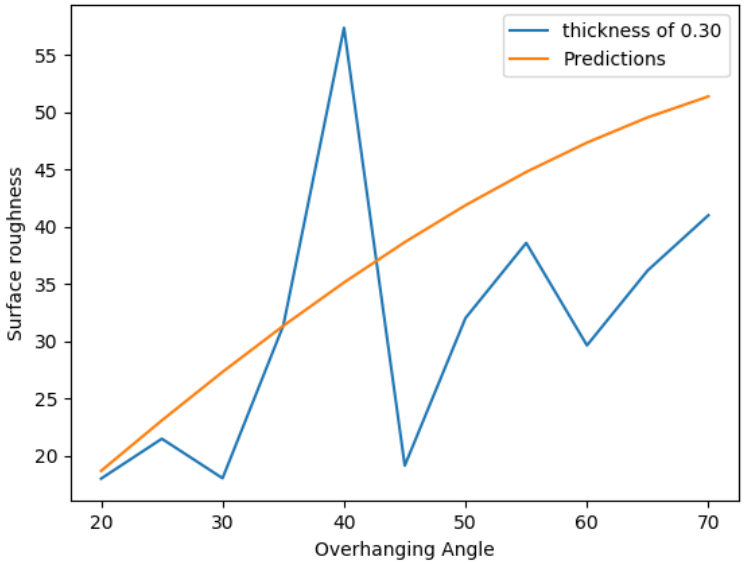

Figure 4.7: Overhanging angle plotted against the surface roughness of down-facing surfaces for a thickness of 0.3 - experimental results in blue, predictions in orange

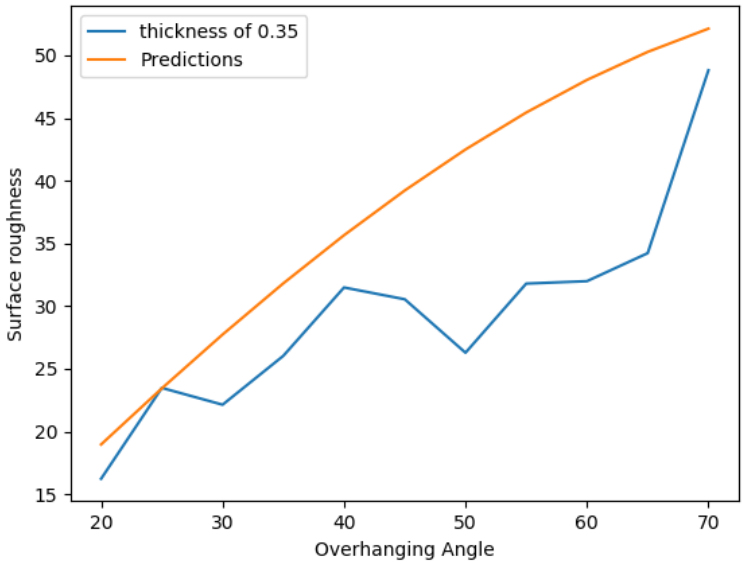

Figure 4.8: Overhanging angle plotted against the surface roughness of down-facing surfaces for a thickness of 0.35 - experimental results in blue, predictions in orange

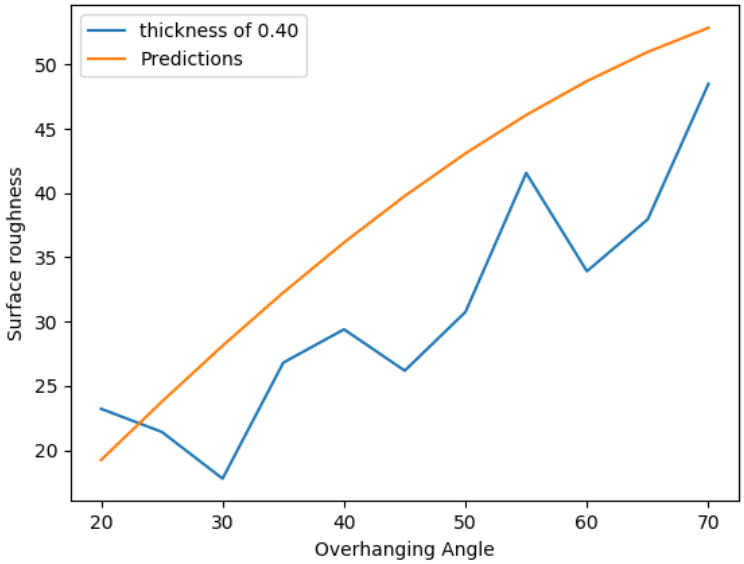

Figure 4.9: Overhanging angle plotted against the surface roughness of down-facing surfaces for a thickness of 0.4 - experimental results in blue, predictions in orange

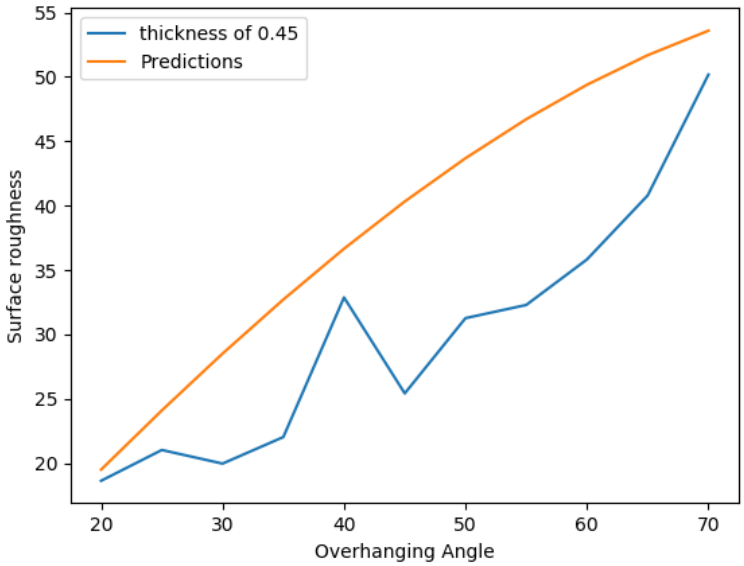

Figure 4.10: Overhanging angle plotted against the surface roughness of down-facing surfaces for a thickness of 0.45 - experimental results in blue, predictions in orange

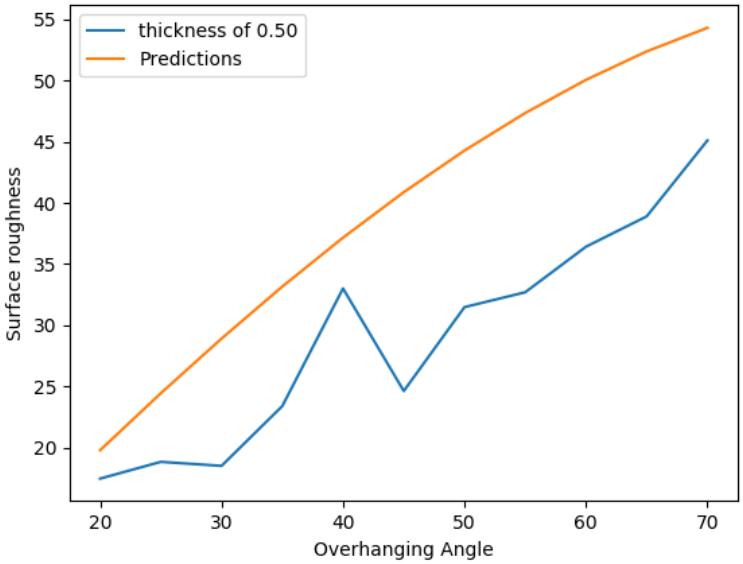

Figure 4.11: Overhanging angle plotted against the surface roughness of down-facing surfaces for a thickness of 0.5 - experimental results in blue, predictions in orange

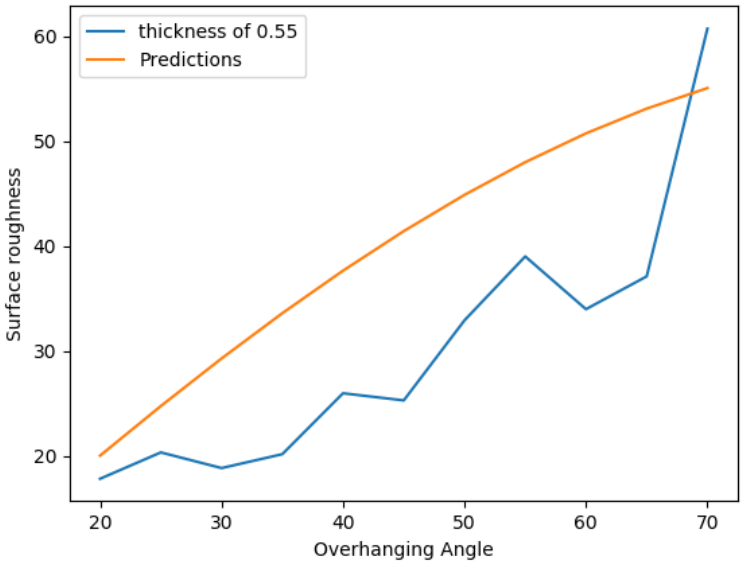

Figure 4.12: Overhanging angle plotted against the surface roughness of down-facing surfaces for a thickness of 0.55 - experimental results in blue, predictions in orange

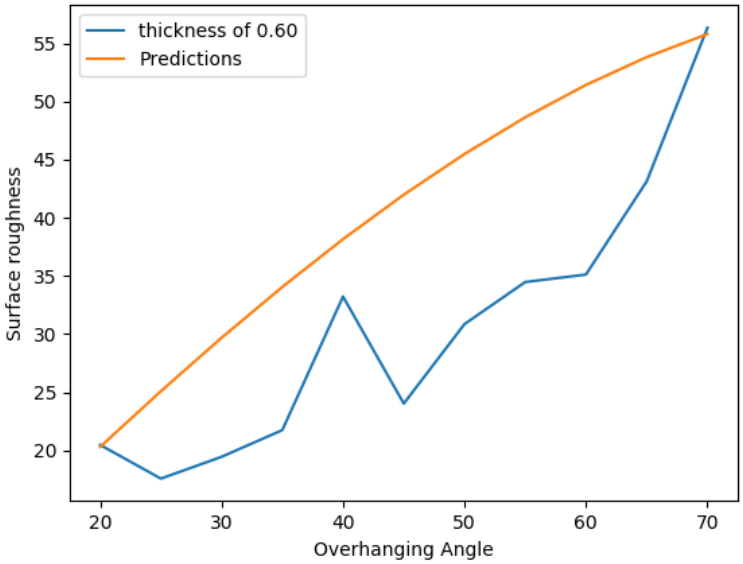

Figure 4.13: Overhanging angle plotted against the surface roughness of down-facing surfaces for a thickness of 0.6 - experimental results in blue, predictions in orange

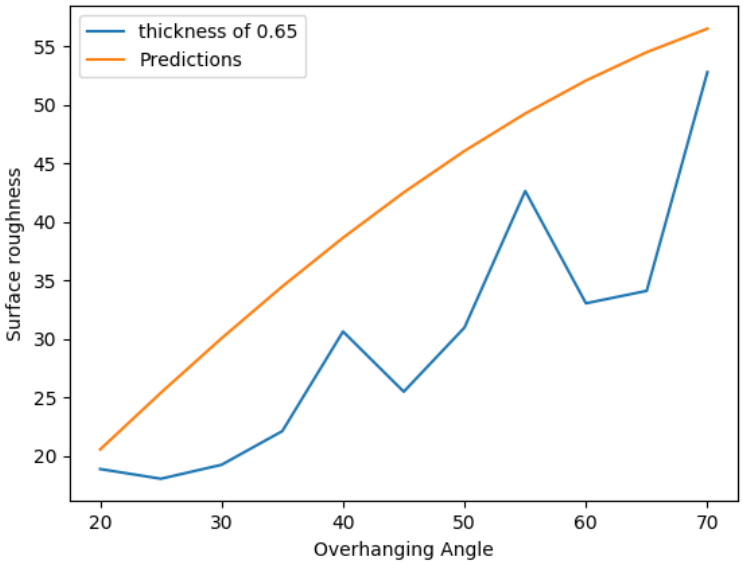

Figure 4.14: Overhanging angle plotted against the surface roughness of down-facing surfaces for a thickness of 0.65 - experimental results in blue, predictions in orange

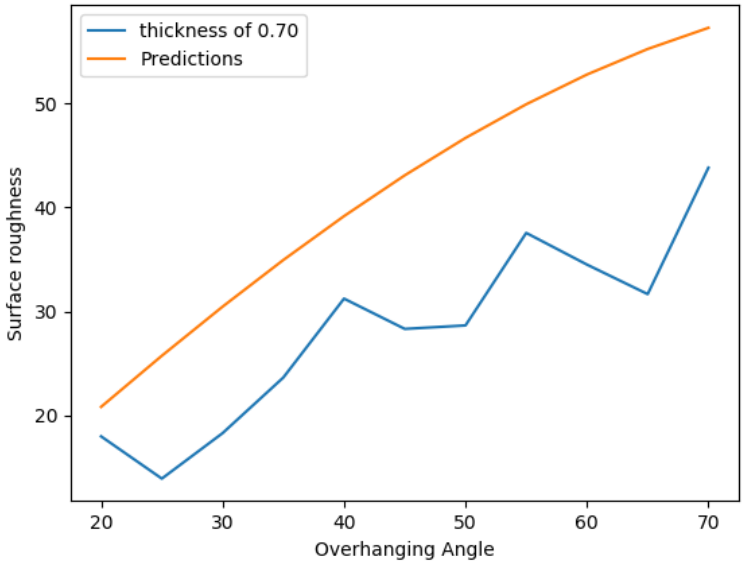

Figure 4.15: Overhanging angle plotted against the surface roughness of down-facing surfaces for a thickness of 0.7 - experimental results in blue, predictions in orange

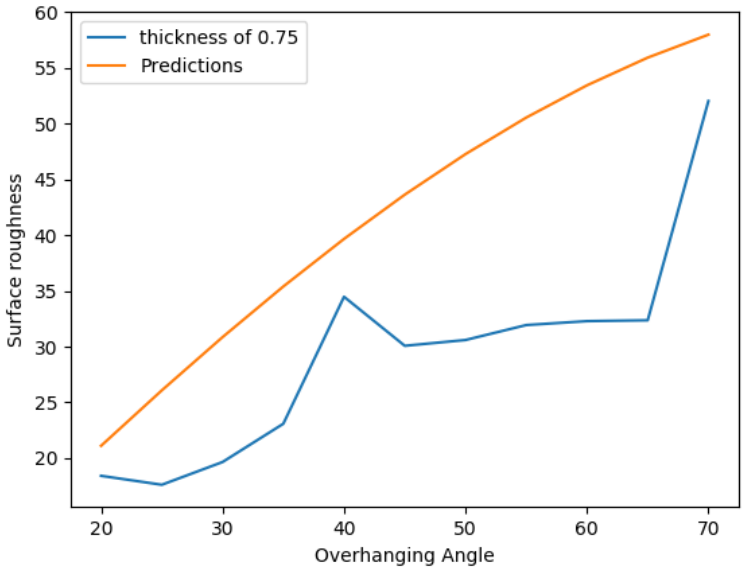

Figure 4.16: Overhanging angle plotted against the surface roughness of down-facing surfaces for a thickness of 0.75 - experimental results in blue, predictions in orange

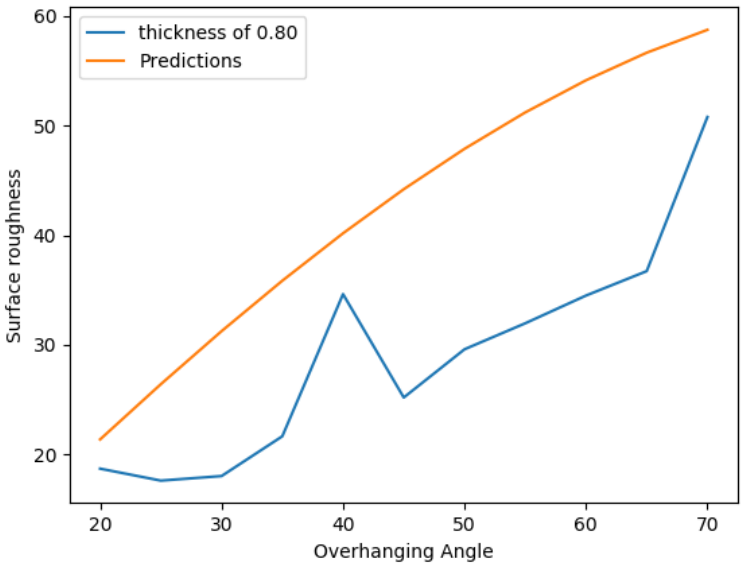

Figure 4.17: Overhanging angle plotted against the surface roughness of down-facing surfaces for a thickness of 0.8 - experimental results in blue, predictions in orange

In general, when few irregularities are put aside, the experimental results seem to follow the trend predicted adequately. It would be interesting to reduce the intervals between successive overhanging angles to have more data and to reject or accept the suggestion properly in future work.

Analysis of variance was performed on the data. The lines and columns referred to the overhanging angles and radii, respectively. It was found that the F value for both lines and columns had passed the critical value test. $F_{lines} = 6.998959$, which was largely above $F_{critical} = 1.910461065$ while $F_{columns} = 2.416596$ which was slightly above its $F_{critical}$ of 1.833695276 and therefore, the OA and the thickness of features were both deemed to be significant factors in the surface roughness of the down-facing surfaces. Furthermore, it also showed that the OA has a larger contribution to determining the surface roughness of the feature's bottom surface than the radii.

Chapter 5

A workflow for altering the layout of existing topologically optimized structures using experimental data

The content in this chapter relies less on physical experiments and more on geometrical analysis. This chapter aims to modify the layout of topologically optimized structures (TOSs) to enhance the quality of their printed design features. The idea stems from the observation that a two-dimensional TOS can be seen as an assembly of struts, which explains the comparison with lattice structures. Therefore, it is possible to control the thickness of those struts based on their orientation. The following chapter will describe the method used to alter the material layout of TOSs, and the case study will show an example of how the method has been used. Altering the structural layout of a TOS is nothing new. Similar methods have been used by others but for different reasons. Zhang et al. [50] have extracted a skeleton from a TOS to impose a maximum and minimum thickness. On the other hand, Mass and Amir[63] have used a skeleton to control the maximum overhanging angle better. They performed two optimizations, one on a truss to remove the struts with a certain inclination and the other to come up with a continuum-based model on which they map their first optimization.

The innovation in the present study lies in the coupling of the feature size and feature orientation. Weiss et al. [8] have coupled the feature size and the feature orientation, but they have used a qualitative metric to characterize manufacturability.

Some examples of topologically optimized structures.

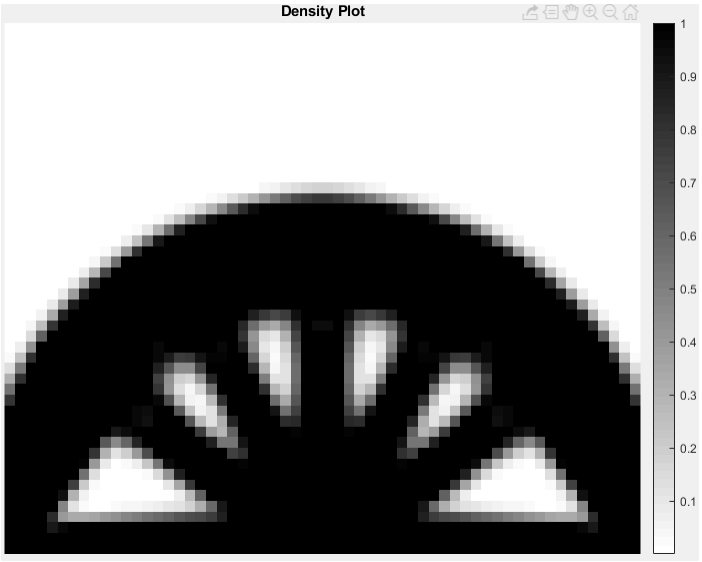

Figure 5.1: TOS with parameters: nelx = 60, nely = 50, volumefrac = 0.5, rmin =2, penalty = 3. The force is applied on the middle node of the bottom row

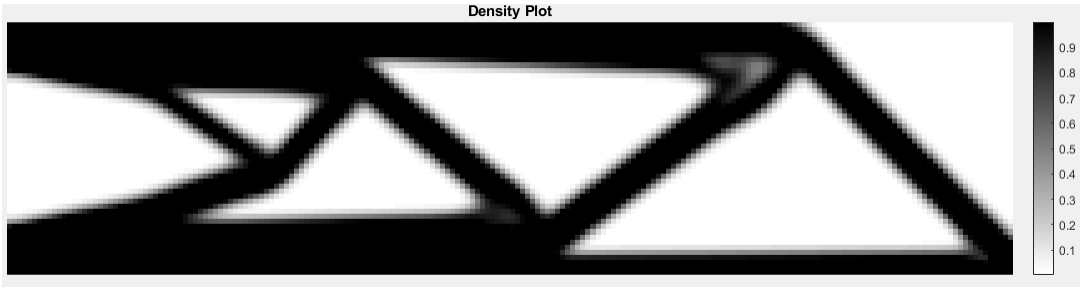

Figure 5.2: TOS with parameters: nelx = 200, nely = 50, volumefrac = 0.5, rmin =3, penalty = 4. The force is applied to the rightmost node of the bottom row

In each of the figures above, nelx and nely refer to the number of elements in the x and y-direction, respectively. Volumefrac is the volume fraction, and rmin is the minimum radius, while penalty is the penalization constant inside the compliance function.

5.1 Methodology

5.1.1 Topology optimization

First, to create the TOS, the 99 line codes from Sigmund[47] and its updated version from Andreassen [52] were used. Sigmund's code works in a set of different steps. At first, the code takes the number of elements in both x and y direction; it also takes a minimum radius, the volume fraction, and a penalty value. As with most gradient-based methods, the program starts by computing the displacements of all nodes using FEA. It then uses the displacement of the nodes to infer the displacement of the elements, which it then uses to update the density of the element and create the sensitivity matrix. The sensitivity matrix is obtained by taking the derivative of the compliance. Then, using the compliance and the sensitivities matrices and the minimum radius, filtering is done for all elements, and the sensitivities are updated. Then, projection is made, and the sensitivities are updated and fed into the optimizer (optimal criteria). The result is an array of pixels in which density varies between 0 and 1. Due to projection, most densities are not uniformly distributed but are rather closer to 0 or 1.

One way to extract a viable skeleton is by using the medial axis.

5.1.2 Medial axis extraction

The medial axis is a shape descriptor heavily used in computer graphics. The medial axis of a 2D shape is the set of all the locations of points inside the shape, which are equidistant to two or more points on the boundary of a shape [84]. There have been a few methods to generate the medial axis over the years [85, 86, 87, 88, 89].

For the current work, the method used will be similar to the method by Aggarwal et al. [87]. The idea is first to extract the contour points of the TOS. To do so, an algorithm was developed. The TOS is passed on to the algorithm as a density matrix of size $nelx \times nely$. Then, once an intensity threshold is fixed (intensity of 0.5 in this case), the algorithm finds the points which follow a specific configuration (as seen in figure 5.3). Each point is a vertex of at most four elements. The corners of the bounding box ($nelx \times nely$) are each only included in one element's vertices, the points on the edges of the bounding box are each the vertices of two elements, and the rest of the points are each the vertices of four elements. Identifying if a point is a contour point comes down to identifying the composition of the elements' density around that point. If the four elements' densities are

above the intensity threshold, then the point is not a contour point. In all other cases, it is. Figure 5.4 shows the contour points of the density matrix from figure 5.1.

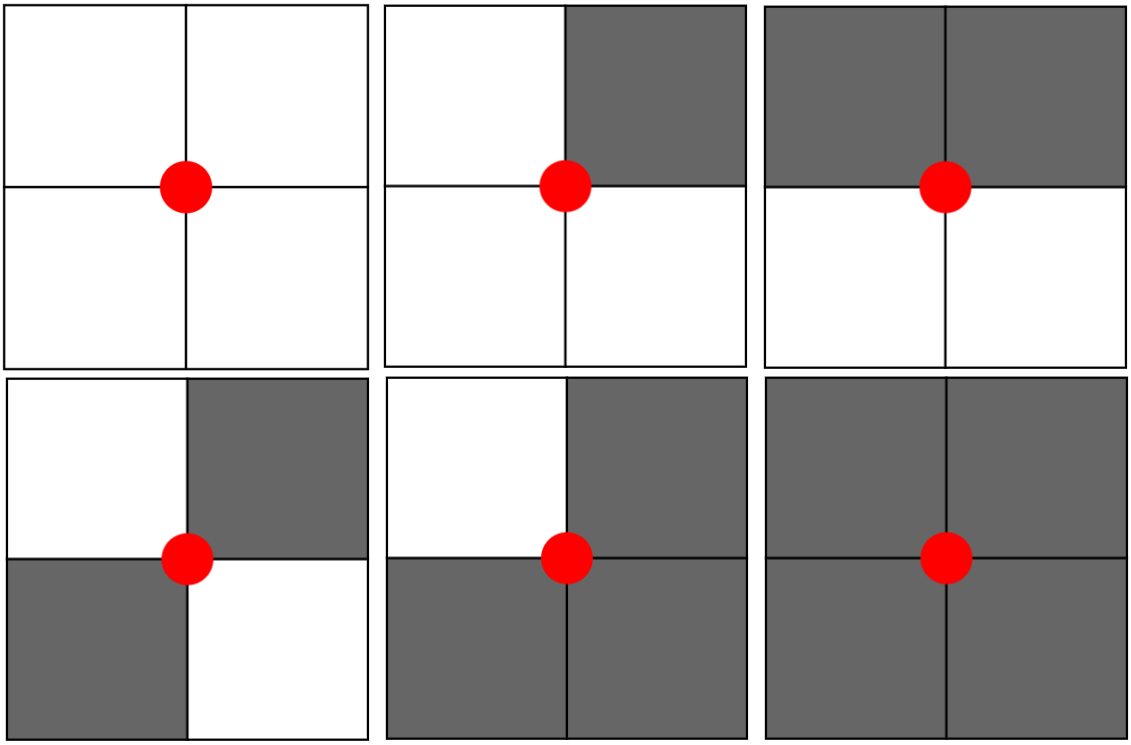

Figure 5.3: Diagram showing all the possible configurations the pixels' densities surrounding a point after considering rotation and mirroring. All cases are contour points except for case 1 and 6

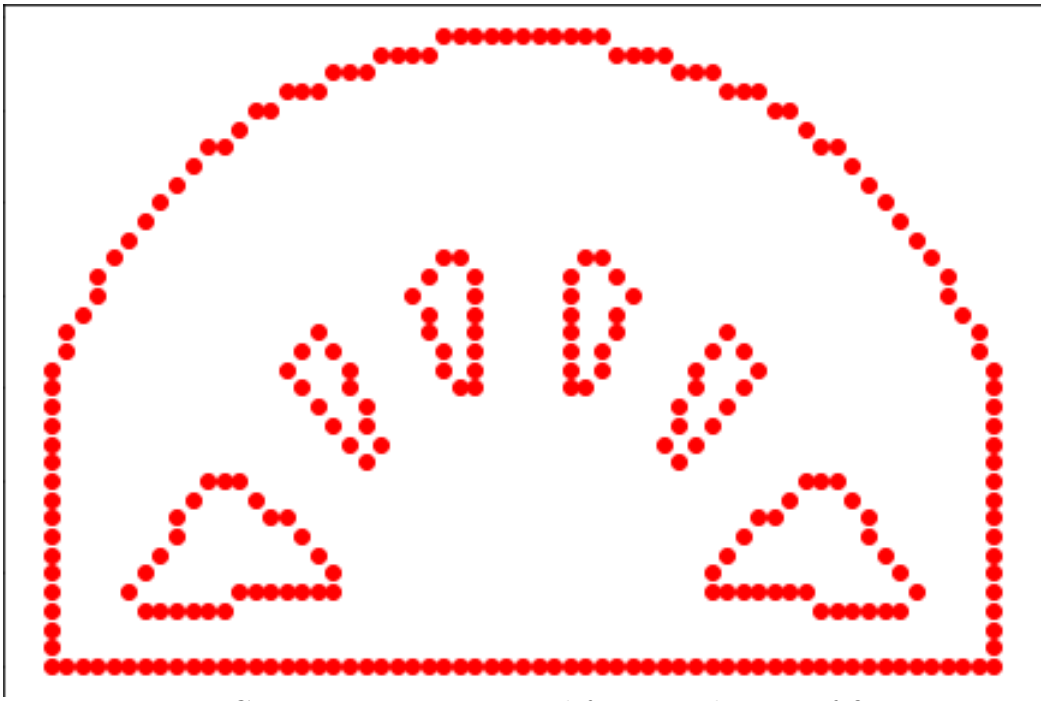

Figure 5.4: Contour points extracted from pixel array of figure 5.1

Once the contour points have been extracted, their Voronoi diagram is computed. The Voronoi diagram was first introduced by Georgy Voronoi [90]. Once given a plane with random points, finding the Voronoi diagram is the equivalent of finding all the edges such that each edge is the set of the locations equidistant from two of the random points (as seen in figure 5.5). The Voronoi diagram was implemented using the Voronoi function from the python scipy library.

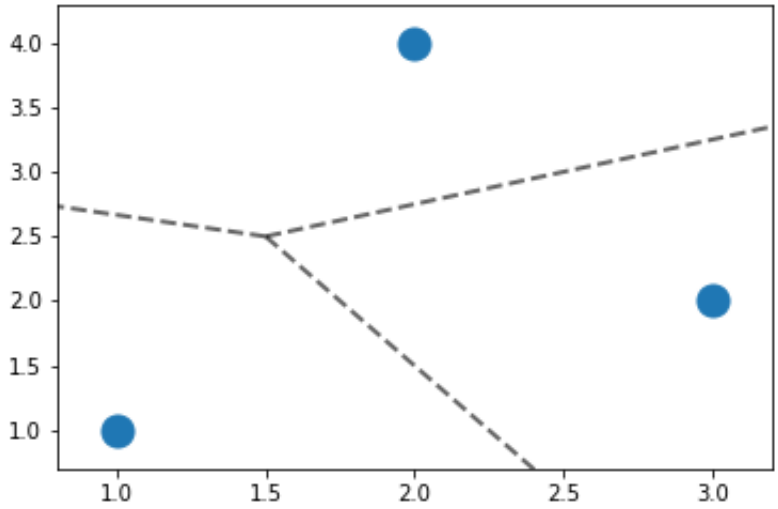

Figure 5.5: Voronoi diagram of 3 points (shown in blue)

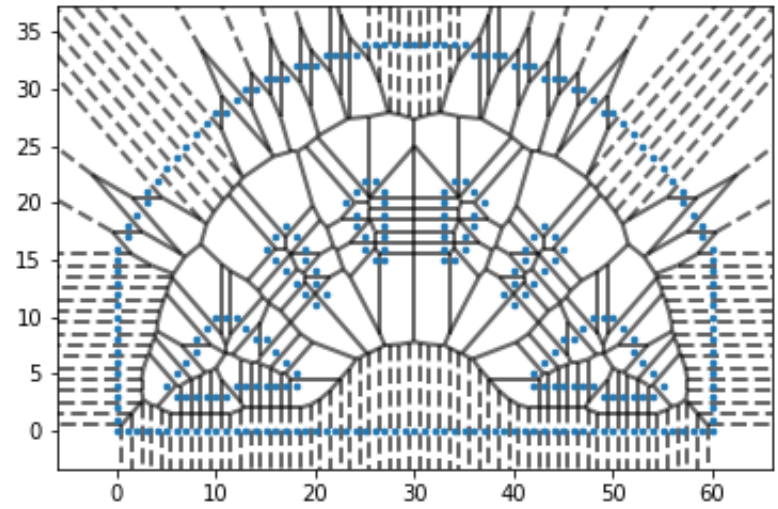

Figure 5.6: Voronoi diagram of the contour points from figure 5.4

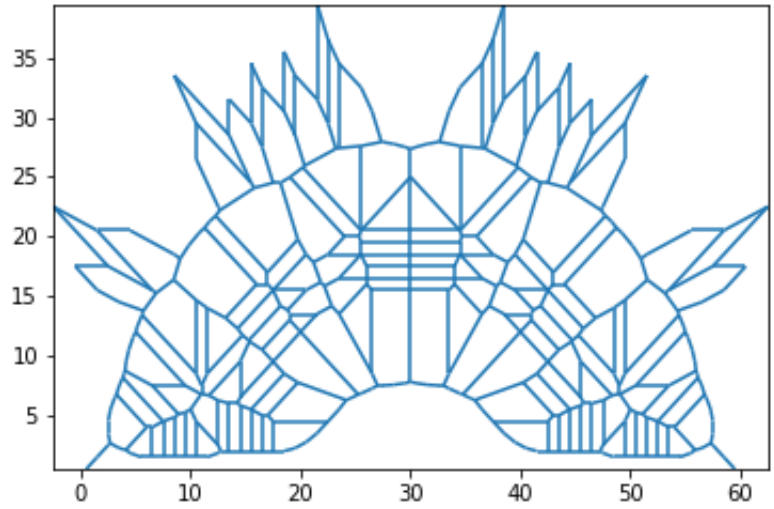

Figure 5.7: Voronoi diagram from figure 5.6 with only the finite edges

In figures 5.5 and 5.6, the dotted lines represent the lines that extend to infinity while the solid lines represent the finite lines. Figure 5.7 shows the result once the dotted lines are removed. The relation between the Voronoi diagram and the medial axis is self-evident; the medial axis of a shape is made up of the of Voronoi edges inside the shape. The next step consists of removing the outer edges from the diagram. To do so, all of the vertices from the Voronoi diagram are examined; if any of the vertices are in an element with a density lower than the threshold (in other words, outside of the shape), the edges connected to that vertex are removed from the edge list. Doing so leads to figure 5.8. When it comes to the medial axis, the curvier the contours, the lower the number of edges in the medial axis. However, this is not the current case. TOSs that use density elements have rough contours depending on how coarse the elements are. The fact that the shape's contour is rough usually leads to a medial axis with a lot of additional edges. Those edges can be dismissed by further processing the shape (figure 5.9).

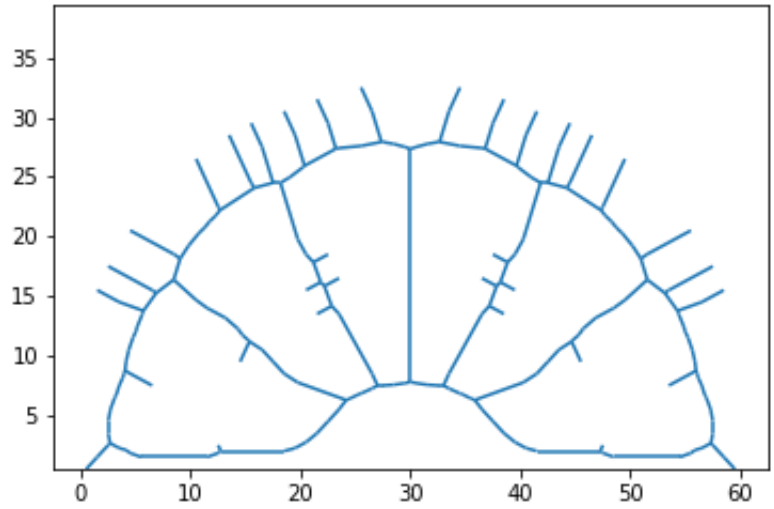

Figure 5.8: Unpolished medial axis

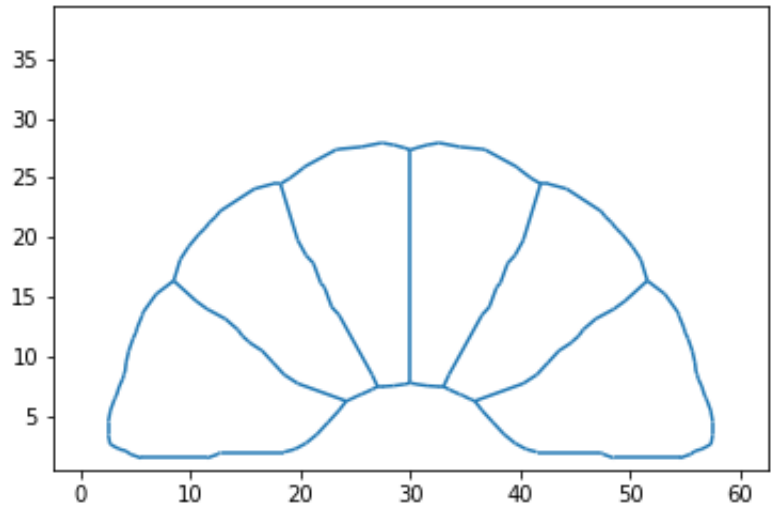

Figure 5.9: Polished medial axis

The result in figure 5.9 is the medial axis or the skeleton of the original image from figure 5.1. Most vertices have degree two (adjacent to two edges), but some have degree

three. Each set of edges between two vertices of degree three is the medial axis of a feature. Each of those sets of edges needs to be smoothed through an additional round of polishing. To do so, the concept of a Bézier curve is used. Bézier curves are curves that are controlled by a set of control points. A linear Bézier curve c(t) is the curve obtained by two points P_0 and P_1 such that:

$$c(t) = P_0 + t \cdot (P_1 - P_0) \tag{5.1}$$
$$c(t) = (1 - t) \cdot P_0 + t \cdot P_1 \tag{5.2}$$

for $0 \leq t \leq 1$. Higher order Bézier curves (which require more than two points) follow the same pattern. Overall, the nth degree Bézier curve can be obtained by the following function:

$$c(t) = \sum_{i=0}^{n} \binom{n}{1} (1 - t)^{n-i} \cdot t^i \cdot P_i \tag{5.3}$$
$$c(t) = \sum_{i=0}^{n} B_i^n \cdot P_i \tag{5.4}$$

Where P_i is the ith control point, n is the number of points and B_i^n is the Bernstein polynomial. Figure 5.10 shows two sets of control points and their respective Bézier curve as examples.

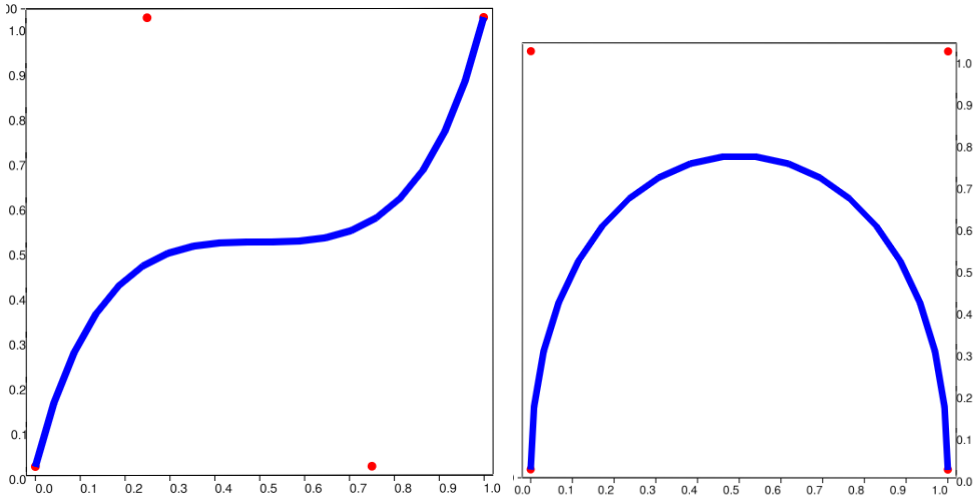

Figure 5.10: Bézier curves(in blue) for different set of control points (in red). In the left picture - (0,0), (0,1) (1,1) and (1,0)- and in the right picture - (0,0), (0.25,1), (0.75,0) and (1,1)

In the current case, each vertex from an internal set of edges is used as a control point. The degree of the different Bézier curves is the number of vertices on the specific medial axis. The final results can be seen in the figures 5.11 and 5.12. Figure 5.13 shows the different members' (or design features') skeletons using separate colors.

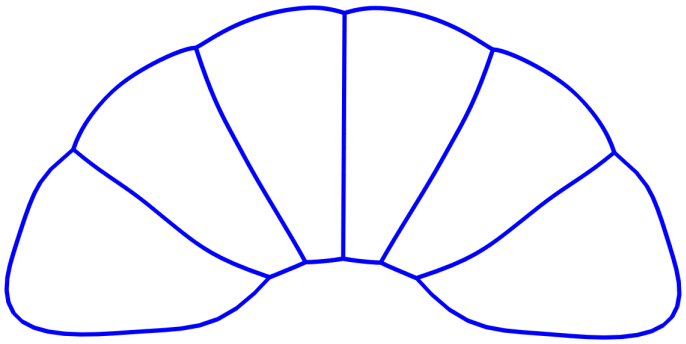

Figure 5.11: Extracted polished and smoothed medial axis from the shape in figure 5.1

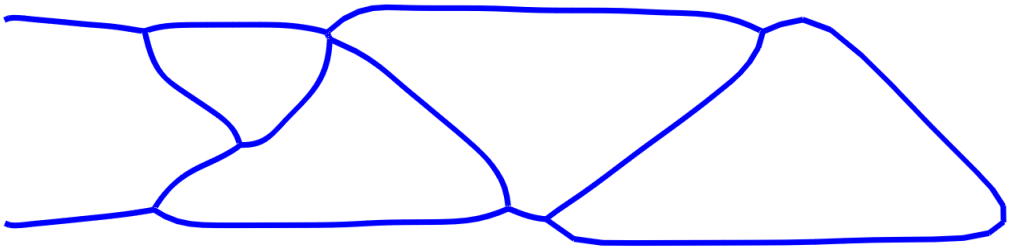

Figure 5.12: Extracted polished and smoothed medial axis from the shape in figure 5.2

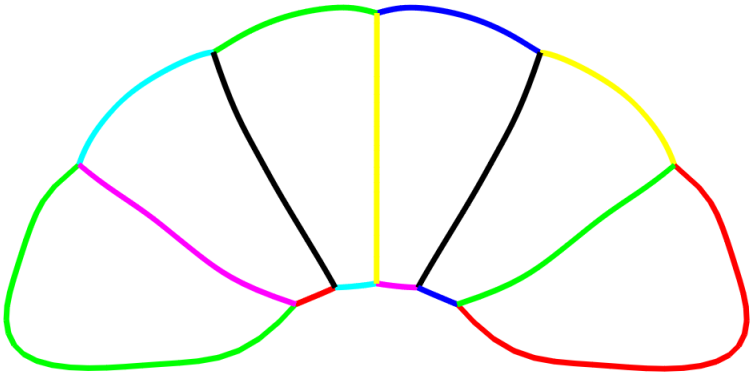

Figure 5.13: The members' skeletons of the figure 5.1

The next step will discuss how the medial axis was thickened based on custom requirements.

5.1.3 Thickening of medial axis

Implicit modeling

Once the medial axis has been smoothed, it can now be thickened. To thicken a medial axis, implicit modeling is used. Implicit modeling is a continuous mathematical representation of an attribute across a volume. It can be used to represent all sorts of shapes through mathematical implicit equations. The advantage of implicit modeling is that primitive shapes can be represented, and it is also easy to create a transition between shapes without creating fillets as it is the case in constructive solid geometry.

Those implicit equations can also be referred to as fields as they can be calculated at every point of the domain. One way to obtain a circular field is by taking the inverse of the function describing that object. Circles are mathematically represented by the equation below:

$$x^2 + y^2 = r^2 \tag{5.5}$$

where r is the circle's radius. The field of a circle will thus be represented by the equation:

$$f = \frac{r^2}{(x^2 + y^2)} \tag{5.6}$$

Superimposing multiple circular fields yields the equation:

$$f(x, y) = \sum_{i=1}^{n} \frac{r_i^2}{((x - x_i)^2 + (y - y_i)^2)^\tau} \tag{5.7}$$

where x_i and y_i are coordinates of the center of the ith circle.τ is a constant that can be adjusted. For figure 5.14, $\tau = \frac{1}{20}$.

Figure 5.14: Superimposition of two circular fields

Figure 5.14 shows the interaction of two circular fields. Both fields contribute to all the pixels' intensities. To extract a practical shape from that space, it is necessary to use isocontours.

Isocontours

Isocontours, the two-dimensional equivalent of isosurfaces, also referred to as level sets, signifies a contour of equal height. The imagery has a lot to do with geography. The same concept can be applied to the current problem by changing the word height to density. By applying isocontours to figure 5.14, one can get a set of non-intersecting curves defining a closed geometry (see figure 5.15). To render such a geometry, there have been a couple of algorithms that have been developed, the most famous one being the marching cubes algorithm by Lorensen [91], and its 2D equivalent, marching squares. The marching square algorithm divides the space into a grid of squares. An iso-value is given, and each vertex of the grid is evaluated using the implicit model. The algorithm generates a set of edges in the squares where at least one vertex is below the iso-value, and at least one vertex is above the iso-value. Controlling the size of the grid allows the user to change the resolution.

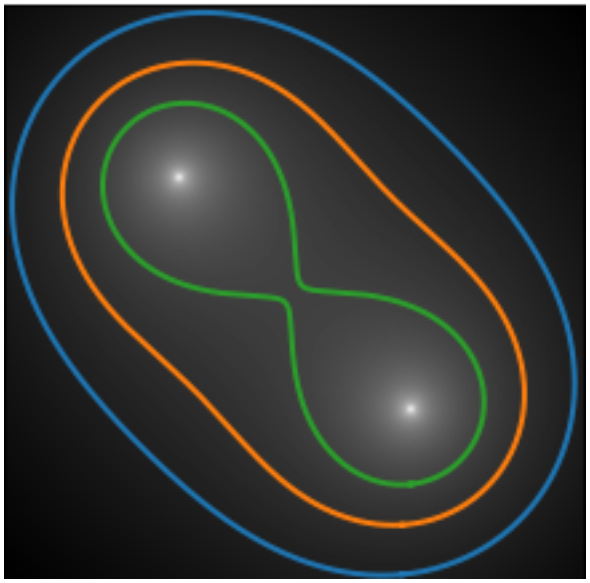

Figure 5.15: Multiple isocontours associated to different iso-values for the figure 5.15- an iso-value of 0.12 for the blue contour, of 0.18 for the orange contour and 0.25 for the green contour. The field values were restricted between 0 and 1.

To apply this concept to the present study, multiple points along each of the Bézier curves obtained earlier were used as the circular fields' centers. The number of points along the curves depended on the size of the curve. Figures 5.16 and 5.17 show the importance of putting the right amount of circular fields along the curves so that an adequate set of contours is found.

Figure 5.16: TOS example when the centers of the circular fields are spaced out. From figure 5.1

Figure 5.17: TOS example when the centers of the circular fields are close to each other. From figure 5.1

Now that it has been shown that the medial axis can be thickened using implicit modeling, the next subsection will discuss how it can be thickened based on custom consideration.

5.1.4 Conditional thickening of medial axis

The advantage of having the medial axis of a shape is that the structure's members' size can be controlled using custom requirements. To change the thickness at any given location of the medial axis, the circular field's radius at that precise location must be changed. For example, one can adjust that radius and make it vary based on the x-coordinate so that features on the right are thicker than features on the left, as shown in figure 5.18.

Figure 5.18: Diagram showing features increasing in thickness as the x-coordinates increase

A more interesting result can be found when trying to vary the thickness of a member based on that member's orientation. To do so, the first and last points of each Bézier

curve are used to measure the slope (the inclination) of a feature. The features' sizes of a structure can thus be varied based on the inclination of that feature (see figure 5.19).

Figure 5.19: Diagram showing features increasing in thickness as the overhanging angle increases

In equation 5.7, the variable τ was introduced. The purpose of the variable τ is to affect the propagation of the field from its center. Figures 5.20 and 5.21 shows that the more τ is increased, the smaller its relative propagation is. This can effectively be used to control the maximum distance that a field can reach.

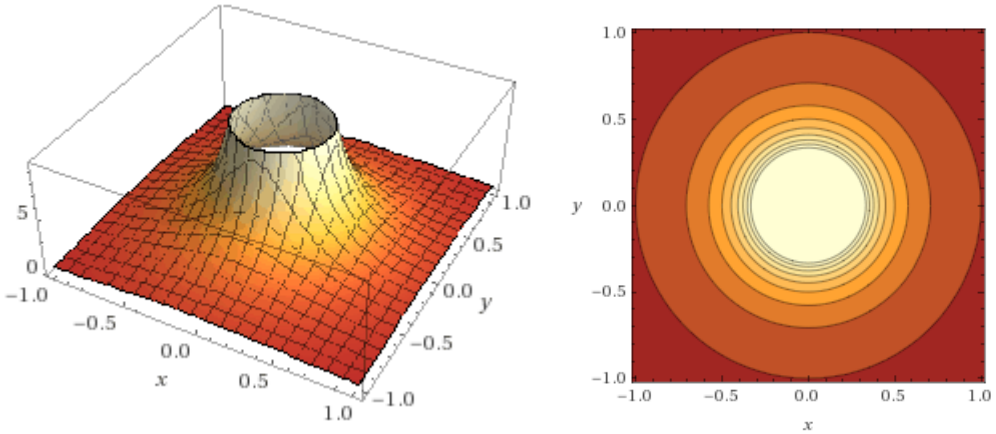

Figure 5.20: Surface and level sets of equation 5.7 for $\tau = 1$

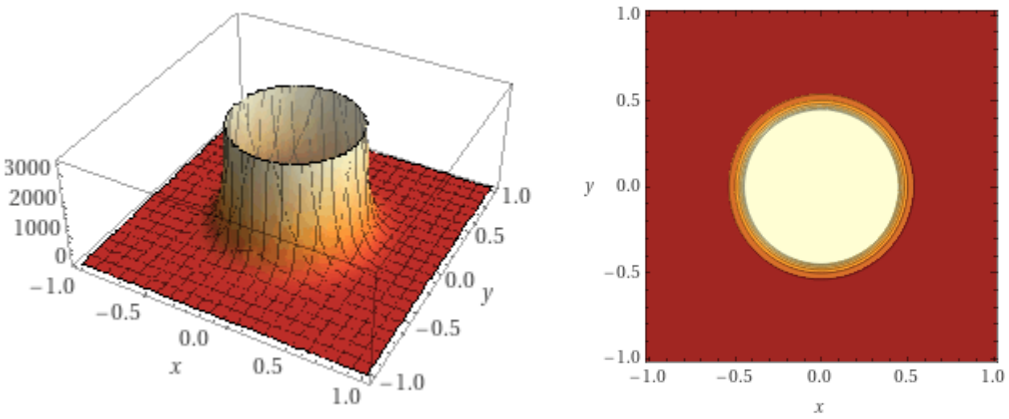

Figure 5.21: Surface and level sets of equation 5.7 for $\tau = 5$

5.2 Case study

The present case study will show the benefits of the methodology developed in section 5.1 of this chapter. The experiments of chapter 3 and 4 will be used to that effect. The main idea behind this case study can be summarized the following way; in chapters 3 and 4, it was shown that the thickness and the orientation of a feature could affect the build quality of that feature. Hence, there is an opportunity: the data from the experiments can be used to infer a rule along which the two parameters of a feature (inclination and thickness) can be restricted.

It can be noticed that for every surface quality value of the 3D graph of figure 4.4, there is a relation between the radius and the overhanging angle. More precisely, a plane parallel to the x-y plane can be drawn at any z value of figure 4.4 to obtain a relation between the minimum feature size and the overhanging angle. However, that relation can be messy due to the irregularities in the 3D plot. Figure 5.22 shows the contour curve, which results from intersecting the plane $z = 29$ (29 is the surface roughness in micrometers). The resulting curve is the equivalent of the isocontour for the iso-value 29.

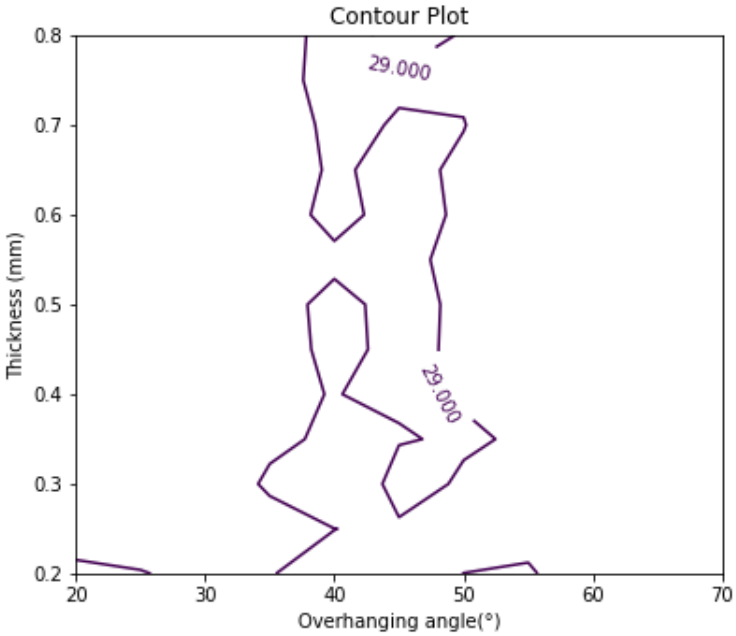

Figure 5.22: Isocontour of the figure 4.4 for an iso-value of 29

To extract anything that makes sense, it is important to approximate the data of the 3D graph.

5.2.1 Surface approximation

To approximate the surface, several methods have been used. Quadratic and quartic surfaces have been used, and the results can be seen in figure 5.23. The "minimize" function from the scipy module has been used to find the polynomial equations' coefficients. The function finds the coefficients that minimize the distance between the polynomial equation and the data points. Two issues arise from this kind of approximation. First, the image of the resulting fitted surface changes highly depending on the initial seed given for the coefficients. Second, the resulting surface is usually an extrusion of a two-dimensional curve, which expresses the surface quality as a function of only the overhanging angle.

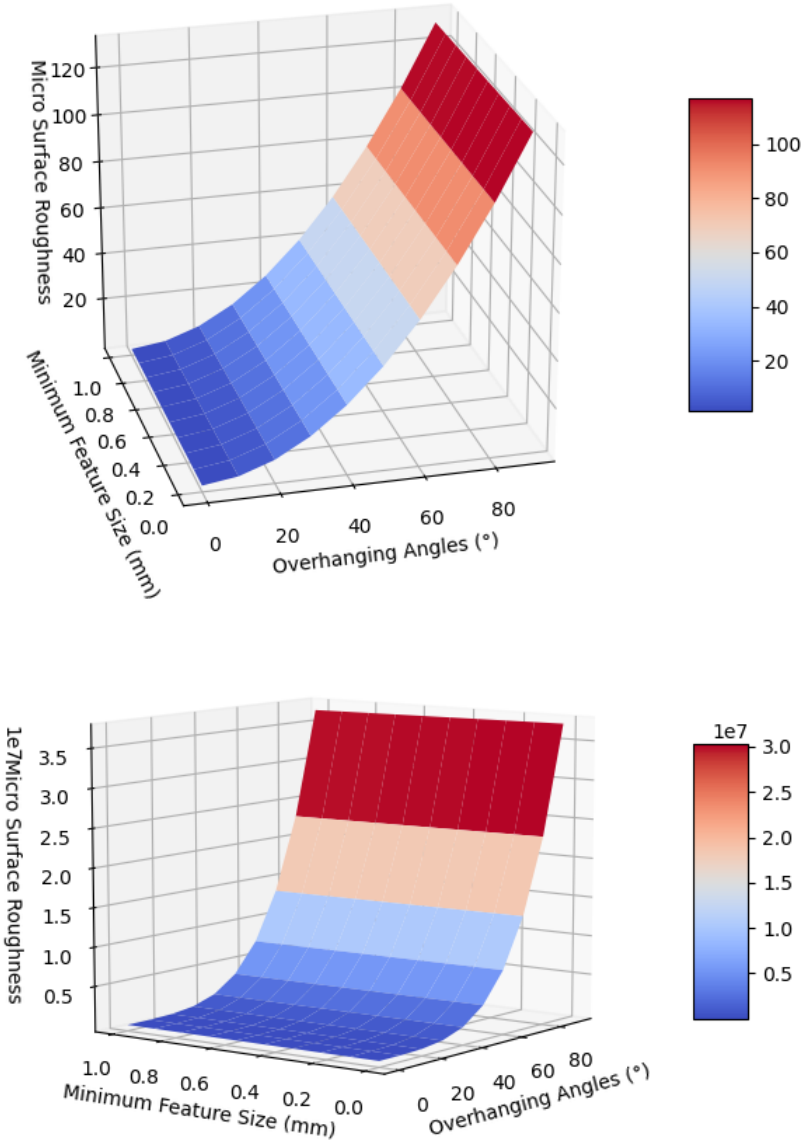

Figure 5.23: Approximation of data points from figure 4.4 using a quadratic surface (top) and a quartic surface (bottom)

To solve this problem, Bézier surfaces were used instead. Bézier surfaces use the same rules as the Bézier curves but in two different dimensions simultaneously, the surface obeys the following equation:

$$s(u,v) = \sum_{i=0}^{n} \sum_{j=0}^{m} B_i^n \cdot B_j^m \cdot P_{i,j} \tag{5.8}$$

where P is the matrix of points and $P_{i,j}$ is the point at location i and j in the matrix and n, and m are the numbers of points both directions. B_i^n and B_j^m are the Bernstein polynomials applied in both directions. The control points used to draw the experimental surface were the ones from the Table 4.1 and figure 4.4.

The final Bézier surface is an approximation of all the data points. The resulting surface can be seen in figure 5.24.

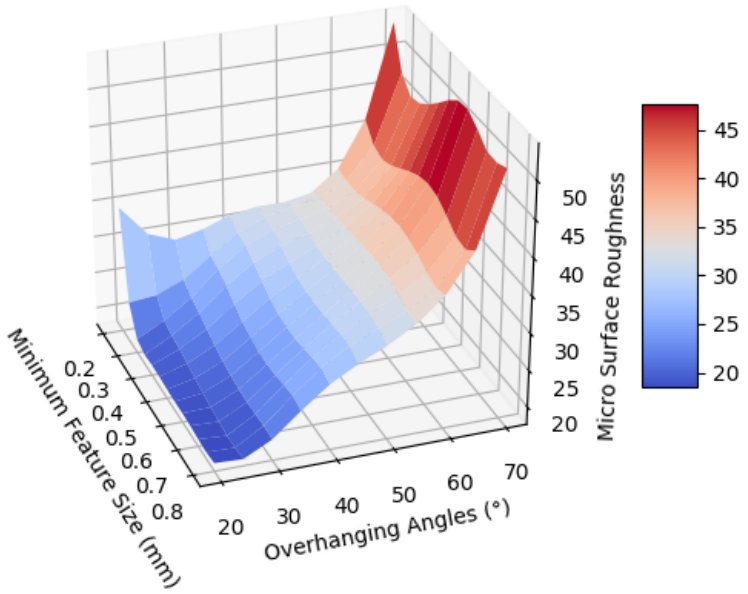

Figure 5.24: Approximation of surface from figure 4.4 using Bézier surface

The advantage of a Bézier surface is that all the points give an equal contribution to the final surface. There is not a single function that describes the surface but rather a set of piece-wise functions. Because various derivatives at each point are taken into consideration, the Bézier surface gives a smooth representation of a trend and lessens the importance of potential outliers that can result from mistakes made during the data acquisition process, consecutively reducing the influence of spikes on the overall surface. Once the surface is

obtained, the same approach as before is performed. If the surface of figure 5.24 is viewed from the top and will result in the heightmap seen in figure 5.25.

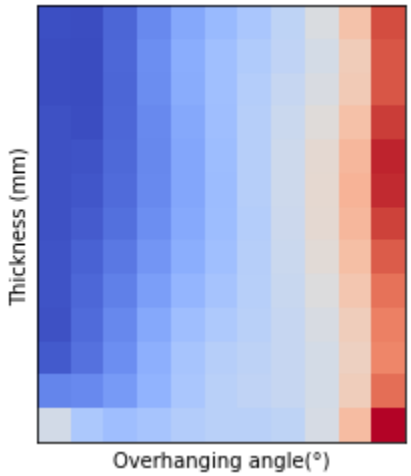

Figure 5.25: Heightmap of the surface from figure 5.24

From that heightmap, isocontours can be generated. The isocontours are seen in figure 5.26.

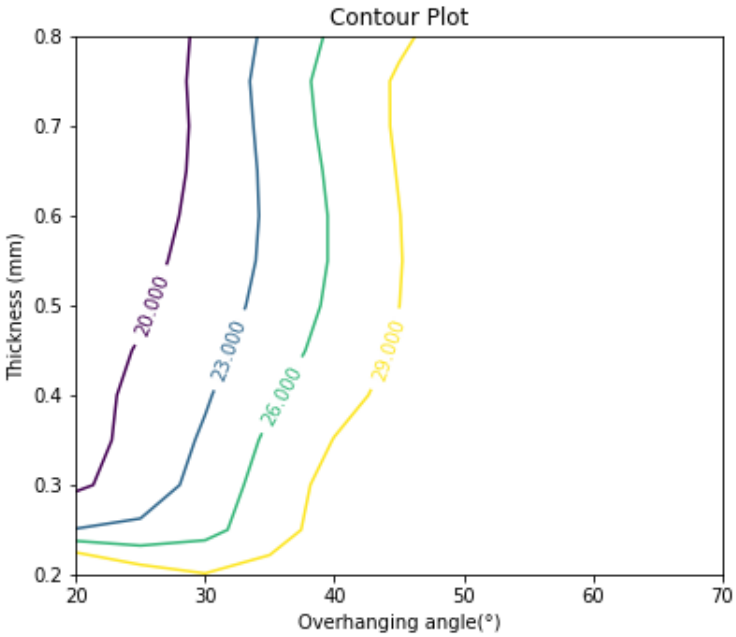

Figure 5.26: Isocountours of heightmap (figure 5.25)

5.2.2 Formula and minimum angle

For the current case study, the isocontour chosen is the one with iso-value 29. To vary the size of the circular field and dictate the feature's size, it is essential to extract a function from the isocontour. Several polynomial functions of different degrees were tried. The one that fitted the most the isocontour was a fourth-degree polynomial otherwise referred to as a quartic polynomial which obeys the equation:

$$r_{min} = a \cdot (\theta - h)^4 + k \tag{5.9}$$

Where r_{min} is the minimum radius. The equation describes a quartic polynomial which extremum is situated at location (h,k). That location refers to the point (20,0.2) and the point (50,0.85) was used to find the value of a. The final equation is:

$$r_{min} = \frac{0.65}{30^4} \cdot (\theta - 20)^4 + 0.2 \tag{5.10}$$

for $\theta \in [0,50]$ and for $r_{min} \in [0,\infty]$. Where θ is the overhanging angle and r_{min} is the minimum allowable thickness. The equation can be seen on figure 5.27.

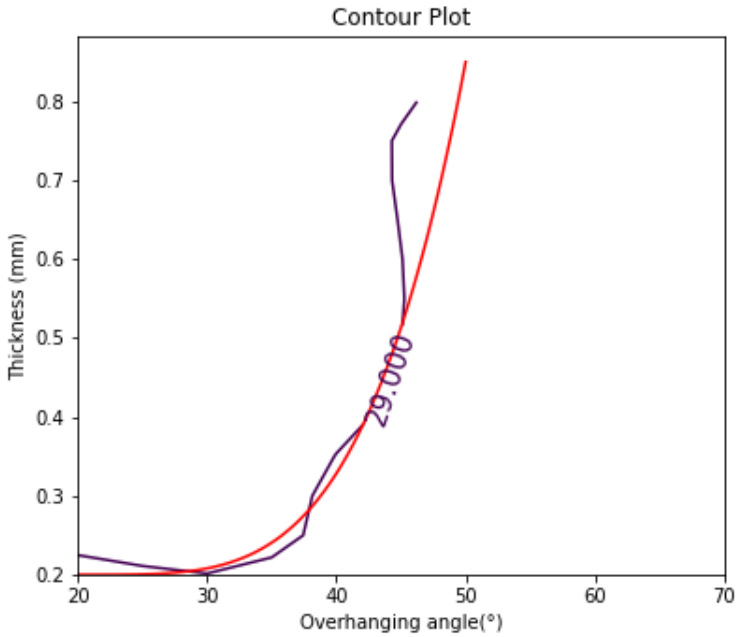

Figure 5.27: Quartic fit of curve (with an iso-value 29) from figure 5.26

5.2.3 Final results

Because the domain of θ is restricted, it is important to restrict the overhanging angle. To do so, a post-processing technique was added to the original solution by Sigmund discussed earlier. The program was written by a colleague. The program adds support structures when an overhang exceeds a certain length.

Figure 5.29 shows the structure for the case study without and with overhanging elimination.

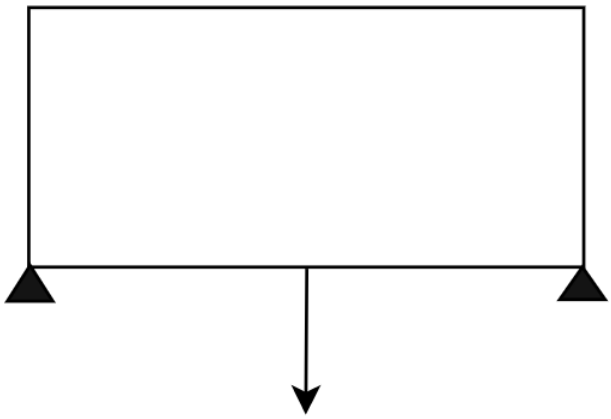

Figure 5.28: Original design space and boundary conditions for the case study

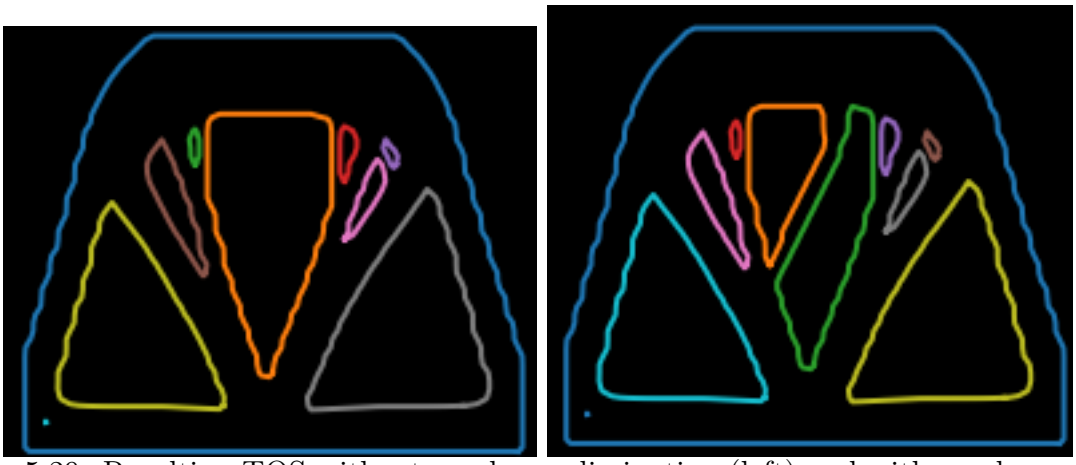

Figure 5.29: Resulting TOS without overhang elimination (left) and with overhang elimination (right)

It can be seen that external supports are added after the optimization to reduce the minimum overhanging angle to 50 °. The rule is applied to the skeleton of the shape to

yield the structures seen in figure 5.32. To generate the thickness, a couple of parameters had to be tweaked. First, a value d had to be used to control the spacing of the centers of the circular fields along the Bézier curves. Then, the value of τ had to be adjusted. Through iteration, it was found that a value τ of 1.2 gives an accurate relative members' width. Finally, the whole radius can be multiplied by a coefficient to scale all the members' width at once.

Figure 5.30: Diagram of the case study altered using quartic fit

The main issue with using this post optimization material layout, instead of relating the r_{min} with the OA during the TO process, is that there are chances that the compliance value will increase. However, it is necessary to reassert that the parts' stress fields follow the direction of the medial axis. Changing the thickness by a reasonable amount should thus not cause a problem when it comes to compliance. However, further studies should be made to determine that.

The difference between the different features' widths may not be extremely visible because quartic curves have a sharp change. This means that for most values below a certain OA, it will have similar results.

To make the change a bit more visible, a linear approximation was taken instead of the quartic one from equation 5.10 (figure 5.31).

The same two points from equation 5.10 were used to generate equation 5.11.

$$r_{min} = \frac{0.65}{30} \cdot (\theta - 20) + 0.2 \tag{5.11}$$

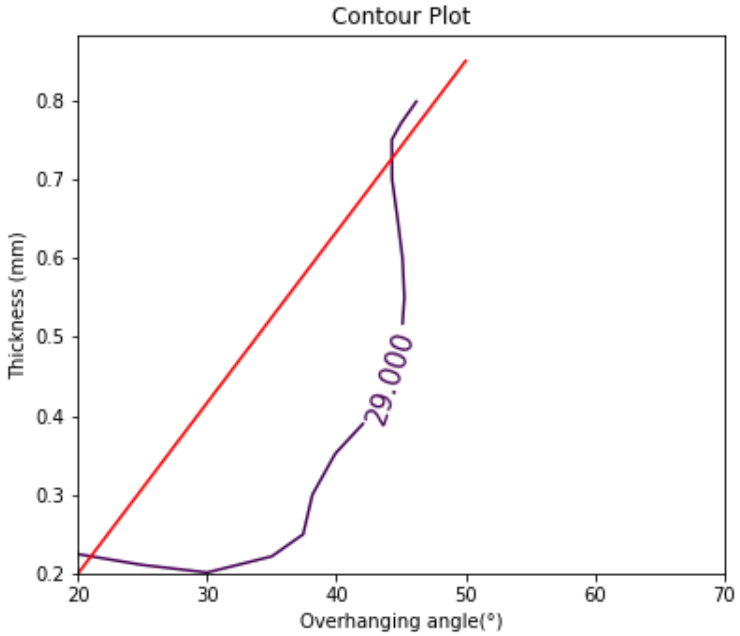

Figure 5.31: Linear fit of curve (with isovalue 29) from figure 5.26

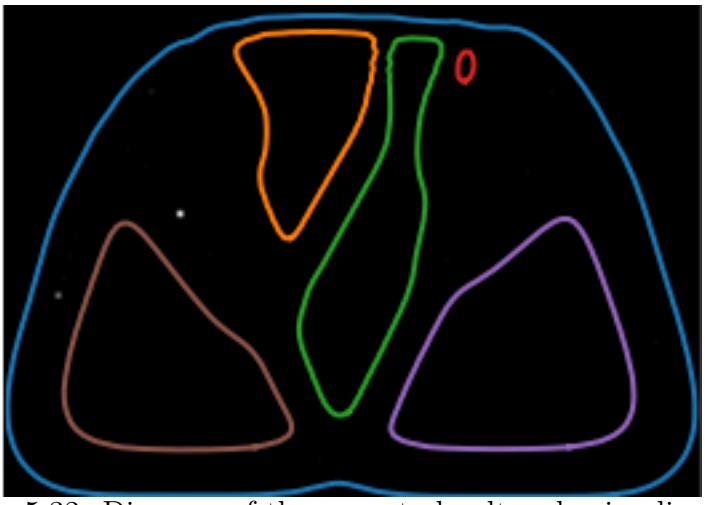

Figure 5.32: Diagram of the case study altered using linear fit

The main difference between figures 5.30 and 5.32 is the overall changes in width. In figure 5.32 the features are usually bigger than the ones in figure 5.30 because of the uniform distribution of feature sizes.

The figures 5.29, 5.30 and 5.32 will show the rendered pictures of the three structures discussed for both case studies. Isocontours were extracted and used to create the final surface. The surfaces were then extruded.

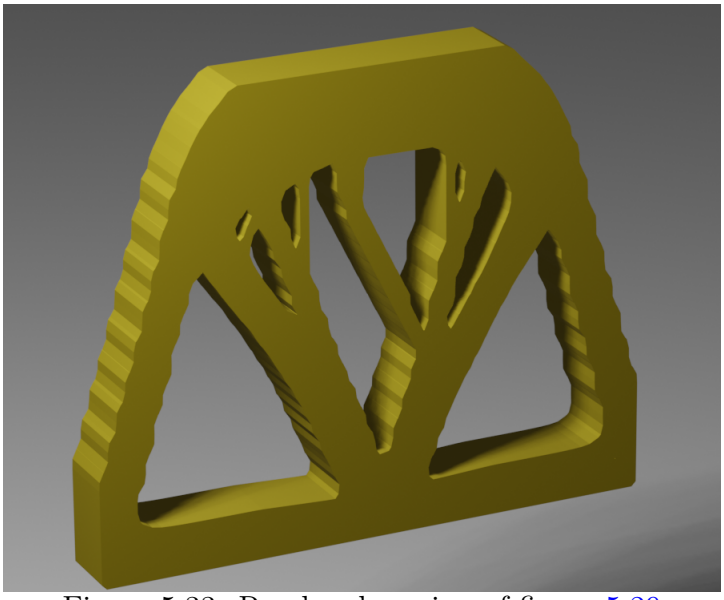

Figure 5.33: Rendered version of figure 5.29

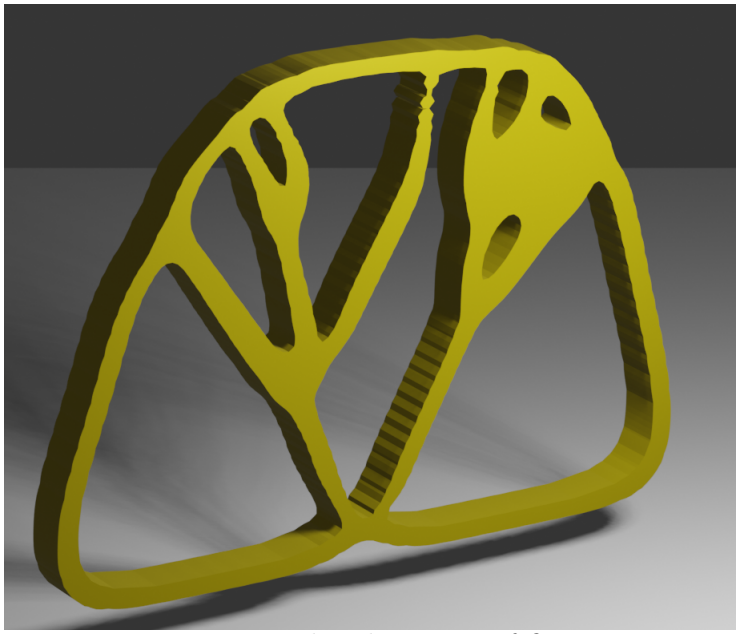

Figure 5.34: Rendered version of figure 5.30

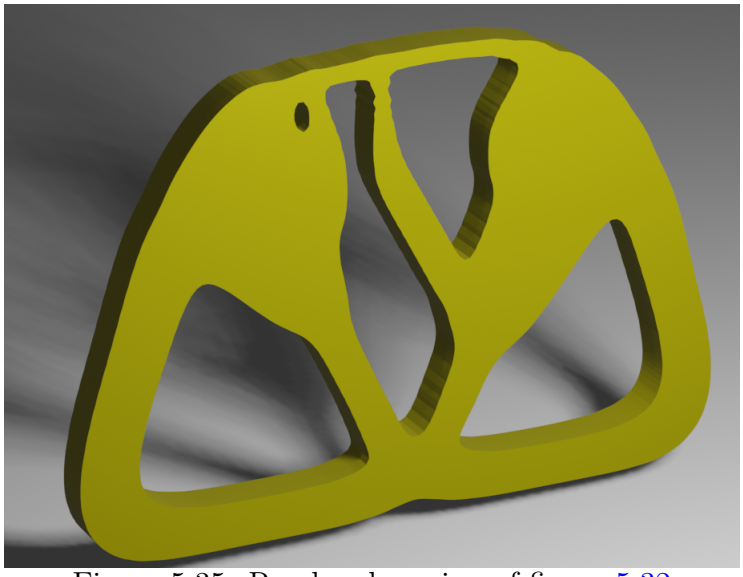

Figure 5.35: Rendered version of figure 5.32

Chapter 6

Conclusions and future work

6.1 Conclusions

To summarize, the work presented here has addressed the importance of considering AM constraints in the design process. It has done so by dividing the study into three separate categories. Two of those categories aim to develop a relationship between design parameters and build quality. In contrast, the last category focused on using the previously derived relationship to alter existing structures. More specifically, the two first categories have qualified and quantified the impact that features' thicknesses and features' orientations have on their down-facing surface roughness. To do so, a couple of oriented struts varying in thickness have been printed and characterized. ANOVA was used to determine that both factors (thickness and orientation) were indeed relevant. The main conclusions to draw from the performed experiments are the following:

- Both the inclination and the thickness affect the surface quality.
- The effect of the parameters is more pronounced for low thicknesses and higher overhanging angles.
- The overhanging angle impacts the surface quality more (the F-value was more than three times the critical F value), which can be seen through ANOVA.

To alter the existing designs using the first categories' results, multiple concepts were borrowed from computer graphics. The medial axis was used to represent the features;

Bézier methods were used to smooth regions of the medial axis and approximate the experimental data. Isocontours were also used twice. Once to extract the relation between inclination and thickness for every surface roughness value, and once again, coupled with implicit functions, to thicken the medial axis. The main conclusions which can be drawn from this part of the work are the following:

- The medial axis is an efficient and elegant way to control the design features parameters.
- Implicit functions can reconstruct the topologically optimized structures, but they require a lot of tuning.

6.2 Future work

The advantage of this work is that it can be transposable to any structure, not only TOSs.Despite the work done in this study, there are still a few things that have to be accomplished.

- For example, it is important to further validate the results by printing the altered TOS.
- It is also necessary to generate more experimental data for LPBF and other AM processes.
- Furthermore, more should be done to study the effect of the layout modification on the compliance.
- Ultimately, more efforts should be geared towards incorporating the results from the experimental data during the topology optimization process and study the effect of the AM constraints on the compliance.

References

[1] Luis E Criales, Yiğit M Arısoy, Brandon Lane, Shawn Moylan, Alkan Donmez, and Tuğrul Özel. Laser powder bed fusion of nickel alloy 625: experimental investigations of effects of process parameters on melt pool size and shape with spatter analysis. *International Journal of Machine Tools and Manufacture*, 121:22–36, 2017.

[2] Sang-in Park and David W Rosen. Quantifying effects of material extrusion additive manufacturing process on mechanical properties of lattice structures using as-fabricated voxel modeling. *Additive Manufacturing*, 12:265–273, 2016.

[3] Mathieu Suard, Guilhem Martin, Pierre Lhuissier, Rémy Dendievel, Frédéric Vignat, J-J Blandin, and François Villeneuve. Mechanical equivalent diameter of single struts for the stiffness prediction of lattice structures produced by electron beam melting. *Additive Manufacturing*, 8:124–131, 2015.

[4] Xinyi Wang, Changdong Zhang, and Tingting Liu. A topology optimization algorithm based on the overhang sensitivity analysis for additive manufacturing. In *IOP Conference Series: Materials Science and Engineering*, volume 382, page 032036. IOP Publishing, 2018.

[5] Pauline Delroisse, Pascal J Jacques, Eric Maire, Olivier Rigo, and Aude Simar. Effect of strut orientation on the microstructure heterogeneities in alsi10mg lattices processed by selective laser melting. *Scripta Materialia*, 141:32–35, 2017.

[6] Elijah Polak. *Optimization: algorithms and consistent approximations*, volume 124. Springer Science & Business Media, 2012.

[7] Benjamin M Weiss, Joshua M Hamel, Duane W Storti, and Mark A Ganter. Towards a general method for constructing manufacturability design rules for an additive manufacturing process. 2019.

[8] Benjamin M Weiss, Joshua M Hamel, Mark A Ganter, and Duane W Storti. Data-driven additive manufacturing constraints for topology optimization. 2018.

[9] Ian Gibson, David W Rosen, Brent Stucker, et al. *Additive manufacturing technologies*, volume 17. Springer, 2014.

[10] William Oropallo and Les A Piegl. Ten challenges in 3d printing. *Engineering with Computers*, 32(1):135–148, 2016.

[11] Guido AO Adam and Detmar Zimmer. Design for additive manufacturing—element transitions and aggregated structures. *CIRP Journal of Manufacturing Science and Technology*, 7(1):20–28, 2014.

[12] I Gibson, G Goenka, R Narasimhan, and N Bhat. Design rules for additive manufacture. In *Solid Freeform Fabrication Symposium*, pages 705–716. University Of Texas Austin, TX, 2010.

[13] M Reza Yavari, Kevin D Cole, and Prahalada K Rao. Design rules for additive manufacturing–understanding the fundamental thermal phenomena to reduce scrap. 2019.

[14] Yuanbin Wang, Robert Blache, Pai Zheng, and Xun Xu. A knowledge management system to support design for additive manufacturing using bayesian networks. *Journal of Mechanical Design*, 140(5), 2018.

[15] Giovanni Strano, Liang Hao, Richard M Everson, and Kenneth E Evans. Surface roughness analysis, modelling and prediction in selective laser melting. *Journal of Materials Processing Technology*, 213(4):589–597, 2013.

[16] Ben Redwood, Filemon Schffer, and Brian Garret. *The 3D printing handbook: technologies, design and applications*. 3D Hubs, 2017.

[17] David J Whitehouse. *Surfaces and their Measurement*. Elsevier, 2004.

[18] Ernest Paul DeGarmo, J Temple Black, Ronald A Kohser, and Barney E Klamecki. *Materials and process in manufacturing*. Prentice Hall Upper Saddle River, 1997.

[19] H Jee, Yan Lu, and P Witherell. Design rules with modularity for additive manufacturing. In *Solid Freeform Fabrication Symposium*, pages 1450–1462, 2015.

[20] Mahesh Mani, Paul Witherell, and Haeseong Jee. Design rules for additive manufacturing: a categorization. In *ASME 2017 International Design Engineering Technical Conferences and Computers and Information in Engineering Conference*. American Society of Mechanical Engineers Digital Collection, 2017.

[21] Sang-In Park, David W Rosen, Seung-kyum Choi, and Chad E Duty. Effective mechanical properties of lattice material fabricated by material extrusion additive manufacturing. *Additive Manufacturing*, 1:12–23, 2014.

[22] Chunlei Qiu, Sheng Yue, Nicholas JE Adkins, Mark Ward, Hany Hassanin, Peter D Lee, Philip J Withers, and Moataz M Attallah. Influence of processing conditions on strut structure and compressive properties of cellular lattice structures fabricated by selective laser melting. *Materials Science and Engineering: A*, 628:188–197, 2015.

[23] Maciej Mazur, Martin Leary, Shoujin Sun, Martin Vcelka, Darpan Shidid, and Milan Brandt. Deformation and failure behaviour of ti-6al-4v lattice structures manufactured by selective laser melting (slm). *The International Journal of Advanced Manufacturing Technology*, 84(5-8):1391–1411, 2016.

[24] Simon Flury, Anne Peutzfeldt, and Adrian Lussi. Influence of surface roughness on mechanical properties of two computer-aided design/computer-aided manufacturing (cad/cam) ceramic materials. *Operative dentistry*, 37(6):617–624, 2012.

[25] Carolyn Conner Seepersad, Janet K Allen, David L McDowell, and Farrokh Mistree. Multifunctional topology design of cellular material structures. *Journal of Mechanical Design*, 130(3):031404, 2008.

[26] Martin P Bendsøe and Ole Sigmund. Material interpolation schemes in topology optimization. *Archive of applied mechanics*, 69(9-10):635–654, 1999.

[27] Mathias Stolpe and Krister Svanberg. An alternative interpolation scheme for minimum compliance topology optimization. *Structural and Multidisciplinary Optimization*, 22(2):116–124, 2001.

[28] Ole Sigmund and Kurt Maute. Topology optimization approaches. *Structural and Multidisciplinary Optimization*, 48(6):1031–1055, 2013.

[29] Xu Guo, Jianhua Zhou, Weisheng Zhang, Zongliang Du, Chang Liu, and Ying Liu. Self-supporting structure design in additive manufacturing through explicit topology optimization. *Computer Methods in Applied Mechanics and Engineering*, 323:27–63, 2017.

[30] Weisheng Zhang, Dong Li, Jian Zhang, and Xu Guo. Minimum length scale control in structural topology optimization based on the moving morphable components (mmc) approach. *Computer Methods in Applied Mechanics and Engineering*, 311:327–355, 2016.

[31] Stanley Osher and James A Sethian. Fronts propagating with curvature-dependent speed: algorithms based on hamilton-jacobi formulations. *Journal of computational physics*, 79(1):12–49, 1988.

[32] Michael Yu Wang, Xiaoming Wang, and Dongming Guo. A level set method for structural topology optimization. *Computer methods in applied mechanics and engineering*, 192(1-2):227–246, 2003.

[33] Grégoire Allaire, François Jouve, and Anca-Maria Toader. Structural optimization using sensitivity analysis and a level-set method. *Journal of computational physics*, 194(1):363–393, 2004.

[34] Simone Cacace, Emiliano Cristiani, and Leonardo Rocchi. A level set based method for fixing overhangs in 3d printing. *Applied Mathematical Modelling*, 44:446–455, 2017.

[35] Jikai Liu and Albert C To. Deposition path planning-integrated structural topology optimization for 3d additive manufacturing subject to self-support constraint. *Computer-Aided Design*, 91:27–45, 2017.

[36] Lu Zhou and Weihong Zhang. Topology optimization method with elimination of enclosed voids. *Structural and Multidisciplinary Optimization*, pages 1–20, 2019.

[37] Weihong Zhang and Lu Zhou. Topology optimization of self-supporting structures with polygon features for additive manufacturing. *Computer Methods in Applied Mechanics and Engineering*, 334:56–78, 2018.

[38] Yuqing Zhou and Kazuhiro Saitou. Topology optimization of composite structures with data-driven resin filling time manufacturing constraint. *Structural and Multidisciplinary Optimization*, 55(6):2073–2086, 2017.

[39] Jiaqi Zhao, Ming Zhang, Yu Zhu, Xin Li, and Leijie Wang. A novel optimization design method of additive manufacturing oriented porous structures. In *ASME 2018 International Mechanical Engineering Congress and Exposition*. American Society of Mechanical Engineers Digital Collection, 2019.

[40] Nicolas Gardan and Alexandre Schneider. Topological optimization of internal patterns and support in additive manufacturing. *Journal of Manufacturing Systems*, 37:417–425, 2015.

[41] Boyan S Lazarov and Fengwen Wang. Maximum length scale in density based topology optimization. *Computer Methods in Applied Mechanics and Engineering*, 318:826–844, 2017.

[42] Kunal Mhapsekar, Matthew McConaha, and Sam Anand. Additive manufacturing constraints in topology optimization for improved manufacturability. *Journal of Manufacturing Science and Engineering*, 140(5):051017, 2018.

[43] Mingdong Zhou, Boyan S Lazarov, Fengwen Wang, and Ole Sigmund. Minimum length scale in topology optimization by geometric constraints. *Computer Methods in Applied Mechanics and Engineering*, 293:266–282, 2015.

[44] Jikai Liu, Yufan Zheng, Rafiq Ahmad, Jinyuan Tang, and Yongsheng Ma. Minimum length scale constraints in multi-scale topology optimisation for additive manufacturing. *Virtual and Physical Prototyping*, 14(3):229–241, 2019.

[45] Mikhail Osanov and James K Guest. Topology optimization for additive manufacturing considering layer-based minimum feature sizes. In *ASME 2017 International Design Engineering Technical Conferences and Computers and Information in Engineering Conference*. American Society of Mechanical Engineers Digital Collection, 2017.

[46] Sandro L Vatanabe, Tiago N Lippi, Cícero R de Lima, Glaucio H Paulino, and Emílio CN Silva. Topology optimization with manufacturing constraints: A unified projection-based approach. *Advances in Engineering Software*, 100:97–112, 2016.

[47] Ole Sigmund. A 99 line topology optimization code written in matlab. *Structural and multidisciplinary optimization*, 21(2):120–127, 2001.

[48] Josephine V Carstensen and James K Guest. Improved two-phase projection topology optimization. In *Proceedings of the 10th World Congress on Structural and Multidisciplinary Optimization, Orlando, Florida*, pages 1–8, 2013.

[49] James K Guest. Topology optimization with multiple phase projection. *Computer Methods in Applied Mechanics and Engineering*, 199(1-4):123–135, 2009.

[50] Weisheng Zhang, Wenliang Zhong, and Xu Guo. An explicit length scale control approach in simp-based topology optimization. *Computer Methods in Applied Mechanics and Engineering*, 282:71–86, 2014.

[51] James K Guest, Jean H Prévost, and Ted Belytschko. Achieving minimum length scale in topology optimization using nodal design variables and projection functions. *International journal for numerical methods in engineering*, 61(2):238–254, 2004.

[52] Erik Andreassen, Anders Clausen, Mattias Schevenels, Boyan S Lazarov, and Ole Sigmund. Efficient topology optimization in matlab using 88 lines of code. *Structural and Multidisciplinary Optimization*, 43(1):1–16, 2011.

[53] Xiaoping Qian. Undercut and overhang angle control in topology optimization: a density gradient based integral approach. *International Journal for Numerical Methods in Engineering*, 111(3):247–272, 2017.

[54] Alain Garaigordobil, Rubén Ansola, Javier Santamaría, and Igor Fernández de Bustos. A new overhang constraint for topology optimization of self-supporting structures in additive manufacturing. *Structural and Multidisciplinary Optimization*, 58(5):2003–2017, 2018.

[55] Sebastián Avelino Gómez Sánchez et al. Topology optimization for additive manufacturing: computing and constraining the overhang angle. 2019.

[56] Davin Jankovics, Hossein Gohari, and Ahmad Barari. Constrained topology optimization for additive manufacturing of structural components in ansys®. 2018.

[57] Andrew T Gaynor and James K Guest. Topology optimization considering overhang constraints: Eliminating sacrificial support material in additive manufacturing through design. *Structural and Multidisciplinary Optimization*, 54(5):1157–1172, 2016.

[58] Matthijs Langelaar. Integrated component-support topology optimization for additive manufacturing with post-machining. *Rapid Prototyping Journal*, 25(2):255–265, 2019.

[59] Yu-Hsin Kuo and Chih-Chun Cheng. Self-supporting structure design for additive manufacturing by using a logistic aggregate function. *Structural and Multidisciplinary Optimization*, pages 1–13, 2019.

[60] Matthijs Langelaar. An additive manufacturing filter for topology optimization of print-ready designs. *Structural and multidisciplinary optimization*, 55(3):871–883, 2017.

[61] Matthijs Langelaar. Topology optimization of 3d self-supporting structures for additive manufacturing. *Additive Manufacturing*, 12:60–70, 2016.

[62] Quhao Li, Wenjiong Chen, Shutian Liu, and Liyong Tong. Structural topology optimization considering connectivity constraint. *Structural and Multidisciplinary Optimization*, 54(4):971–984, 2016.

[63] Yoram Mass and Oded Amir. Topology optimization for additive manufacturing: Accounting for overhang limitations using a virtual skeleton. *Additive Manufacturing*, 18:58–73, 2017.

[64] AM Driessen. Overhang constraint in topology optimisation for additive manufacturing: a density gradient based approach. 2016.

[65] Martin Leary, Luigi Merli, Federico Torti, Maciej Mazur, and Milan Brandt. Optimal topology for additive manufacture: A method for enabling additive manufacture of support-free optimal structures. *Materials & Design*, 63:678–690, 2014.

[66] C-J Thore, H Alm Grundström, Bo Torstenfelt, and Anders Klarbring. Penalty regulation of overhang in topology optimization for additive manufacturing. *Structural and Multidisciplinary Optimization*, 60(1):59–67, 2019.

[67] Amir M Mirzendehdel and Krishnan Suresh. Support structure constrained topology optimization for additive manufacturing. *Computer-Aided Design*, 81:1–13, 2016.

[68] Terrence E Johnson and Andrew T Gaynor. Three-dimensional projection-based topology optimization for prescribed-angle self-supporting additively manufactured structures. *Additive Manufacturing*, 24:667–686, 2018.

[69] Kaiqing Zhang, Gengdong Cheng, and Liang Xu. Topology optimization considering overhang constraint in additive manufacturing. *Computers & Structures*, 212:86–100, 2019.

[70] Emiel van de Ven, Robert Maas, Can Ayas, Matthijs Langelaar, and Fred van Keulen. Continuous front propagation-based overhang control for topology optimization with additive manufacturing. *Structural and Multidisciplinary Optimization*, 57(5):2075–2091, 2018.

[71] Hao Zhou, Junyuan Zhang, Yuqing Zhou, and Kazuhiro Saitou. Multi-component topology optimization for die casting (mto-d). *Structural and Multidisciplinary Optimization*, pages 1–15, 2019.

[72] Gustavo Assis da Silva, André Teófilo Beck, and Ole Sigmund. Stress-constrained topology optimization considering uniform manufacturing uncertainties. *Computer Methods in Applied Mechanics and Engineering*, 344:512–537, 2019.

[73] S Sikder, Ahmad Barari, and HA Kishawy. Effect of adaptive slicing on surface integrity in additive manufacturing. In *ASME 2014 International Design Engineering Technical Conferences and Computers and Information in Engineering Conference*, pages V01AT02A052–V01AT02A052. American Society of Mechanical Engineers, 2014.

[74] F Calignano. Investigation of the accuracy and roughness in the laser powder bed fusion process. *Virtual and Physical Prototyping*, 13(2):97–104, 2018.

[75] Chunze Yan, Liang Hao, Ahmed Hussein, Simon Lawrence Bubb, Philippe Young, and David Raymont. Evaluation of light-weight alsi10mg periodic cellular lattice structures fabricated via direct metal laser sintering. *Journal of Materials Processing Technology*, 214(4):856–864, 2014.

[76] Chunze Yan, Liang Hao, Ahmed Hussein, and David Raymont. Evaluations of cellular lattice structures manufactured using selective laser melting. *International Journal of Machine Tools and Manufacture*, 62:32–38, 2012.

[77] Swee Leong Sing, Florencia Edith Wiria, and Wai Yee Yeong. Selective laser melting of lattice structures: A statistical approach to manufacturability and mechanical behavior. *Robotics and Computer-Integrated Manufacturing*, 49:170 – 180, 2018.

[78] Anton Du Plessis, Igor Yadroitsev, Ina Yadroitsava, and Stephan G Le Roux. X-ray microcomputed tomography in additive manufacturing: a review of the current technology and applications. *3D Printing and Additive Manufacturing*, 5(3):227–247, 2018.

[79] Saad A Khairallah, Andrew T Anderson, Alexander Rubenchik, and Wayne E King. Laser powder-bed fusion additive manufacturing: Physics of complex melt flow and formation mechanisms of pores, spatter, and denudation zones. *Acta Materialia*, 108:36–45, 2016.

[80] YJ Liu, XP Li, Laichang C Zhang, and TB Sercombe. Processing and properties of topologically optimised biomedical ti–24nb–4zr–8sn scaffolds manufactured by selective laser melting. *Materials Science and Engineering: A*, 642:268–278, 2015.

[81] S. L. Sing, W. Y. Yeong, F. E. Wiria, and B. Y. Tay. Characterization of titanium lattice structures fabricated by selective laser melting using an adapted compressive test method. *Experimental Mechanics*, 56(5):735–748, Jun 2016.

[82] Chunlei Qiu, Chinnapat Panwisawas, Mark Ward, Hector C Basoalto, Jeffery W Brooks, and Moataz M Attallah. On the role of melt flow into the surface structure and porosity development during selective laser melting. *Acta Materialia*, 96:72–79, 2015.

[83] H Abramovitch, M Burgard, Lucy Edery-Azulay, KE Evans, M Hoffmeister, W Miller, F Scarpa, CW Smith, and Kong-Fah Tee. Smart tetrachiral and hexachiral honeycomb: Sensing and impact detection. *Composites Science and Technology*, 70(7):1072–1079, 2010.

[84] Harry Blum et al. *A transformation for extracting new descriptors of shape*, volume 4. MIT press Cambridge, 1967.

[85] Franco P Preparata. The medial axis of a simple polygon. In *International Symposium on Mathematical Foundations of Computer Science*, pages 443–450. Springer, 1977.

[86] Der-Tsai Lee. Medial axis transformation of a planar shape. *IEEE Transactions on pattern analysis and machine intelligence*, (4):363–369, 1982.

[87] Alok Aggarwal, Leonidas J Guibas, James Saxe, and Peter W Shor. A linear-time algorithm for computing the voronoi diagram of a convex polygon. *Discrete & Computational Geometry*, 4(6):591–604, 1989.

[88] Rolf Klein and Andrzej Lingas. A linear-time randomized algorithm for the bounded voronoi diagram of a simple polygon. *International Journal of Computational Geometry & Applications*, 6(03):263–278, 1996.

[89] Francis Chin and Cao An Wang. Finding the constrained delaunay triangulation and constrained voronoi diagram of a simple polygon in linear time. *SIAM Journal on Computing*, 28(2):471–486, 1998.

[90] Martin Erwig. The graph voronoi diagram with applications. *Networks: An International Journal*, 36(3):156–163, 2000.

[91] William E Lorensen and Harvey E Cline. Marching cubes: A high resolution 3d surface construction algorithm. In *ACM siggraph computer graphics*, volume 21, pages 163–169. ACM, 1987.